ADVANCED MATERIALS
www.advmat.de

Assessing Biomaterial-Induced Stem Cell Lineage Fate by Machine Learning-Based Artificial Intelligence

Yingying Zhou, Xianfeng Ping, Yusi Guo, Boon Chin Heng, Yijun Wang, Yanze Meng, Shengjie Jiang, Yan Wei, Binbin Lai, Xuehui Zhang,* and Xuliang Deng**

Current functional assessment of biomaterial-induced stem cell lineage fate in vitro mainly relies on biomarker-dependent methods with limited accuracy and efficiency. Here a "Mesenchymal stem cell Differentiation Prediction (MeD-P)" framework for biomaterial-induced cell lineage fate prediction is reported. MeD-P contains a cell-type-specific gene expression profile as a reference by integrating public RNA-seq data related to tri-lineage differentiation (osteogenesis, chondrogenesis, and adipogenesis) of human mesenchymal stem cells (hMSCs) and a predictive model for classifying hMSCs differentiation lineages using the k-nearest neighbors (kNN) strategy. It is shown that MeD-P exhibits an overall accuracy of 90.63% on testing datasets, which is significantly higher than the model constructed based on canonical marker genes (80.21%). Moreover, evaluations of multiple biomaterials show that MeD-P provides accurate prediction of lineage fate on different types of biomaterials as early as the first week of hMSCs culture. In summary, it is demonstrated that MeD-P is an efficient and accurate strategy for stem cell lineage fate prediction and preliminary biomaterial functional evaluation.

1. Introduction

Biomaterials can be fabricated with a variety of different physicochemical factors that could efficiently induce stem cells into designated cell lineages through various complex regulatory mechanisms.[1] Mesenchymal stem cells (MSCs), which possess self-renewal capacity and multi-lineage differentiation potential, are currently the most commonly utilized stem cell type in tissue engineering.[2] The performance assessment on regulating directional MSCs lineage fate is considered to be a key aspect in the overall evaluation of biomaterials in the treatment of tissue defects arising from trauma, inflammatory diseases, or metabolic disorders.[3] For example, precise regulation of lineage fate by biomaterials could lead to MSCs differentiating toward osteoblast/chondrocyte progenitors within osteochondral defects at the right time and place.[4]

Nevertheless, research progress in this area is being impeded by limitations of conventional techniques in evaluating the induction efficiency of stem cell lineage commitment, which are time-consuming, labor-intensive, and uneconomical.[5] Examples include microscopic observations with various staining techniques, flow cytometry, polymerase chain reaction (PCR), and Western Blots, which evaluate lineage-specific differentiation by identifying specific biomarkers of known cell types.[6] Next-generation sequencing (NGS) is also widely used due to its high throughput capacity.[7] Stem cell lineage fate can be predicted by functional bioinformatics analysis. However, results based on current methods can be affected by many factors, such as different laboratory apparatuses and reagent resources and the varying skill levels of operators.[8] Consequently, it is difficult to directly compare data generated from different laboratories. Moreover, tedious normalization is required to analyze data across different materials or on

Y. Zhou, Y. Wang, Y. Meng, X. Zhang
Department of Dental Materials and Dental Medical Devices Testing Center
Peking University School and Hospital of Stomatology
Beijing 100081, P. R. China
E-mail: zhangxuehui@bjmu.edu.cn

Y. Zhou, X. Ping, Y. Guo, B. C. Heng, Y. Wang, Y. Meng, S. Jiang, Y. Wei, X. Zhang, X. Deng
National Engineering Research Center of Oral Biomaterials and Digital Medical Devices
NMPA Key Laboratory for Dental Materials
Beijing Laboratory of Biomedical Materials
Peking University School and Hospital of Stomatology
Beijing 100081, P. R. China
E-mail: kqdengxuliang@bjmu.edu.cn

The ORCID identification number(s) for the author(s) of this article can be found under https://doi.org/10.1002/adma.202210637.

DOI: 10.1002/adma.202210637

X. Ping, B. C. Heng
Central Laboratory
Peking University School and Hospital of Stomatology
Beijing 100081, P. R. China

Y. Guo, S. Jiang, Y. Wei, X. Deng
Department of Geriatric Dentistry
Peking University School and Hospital of Stomatology
Beijing 100081, P. R. China

B. Lai, X. Deng
Biomedical Engineering Department
Peking University
Beijing 100191, P. R. China
E-mail: laib@bjmu.edu.cn

B. Lai
Department of Dermatology and Venereology
Peking University First Hospital
Beijing 100034, P. R. China

 © 2023 Wiley-VCH GmbH

different batches of the same material. Hence, there is a dire need for a more efficient, accurate and convenient method that supports cross-laboratory, inter-material, and batch-independent comparisons for functional evaluation of biomaterials.

To overcome these challenges, the application of artificial intelligence in biomedicine may be particularly useful, as this has advanced greatly in recent years.[9] Several studies have reported that machine learning can be used to make precise predictions. Recent findings suggested that machine learning could recognize morphological changes from microscopy images and subsequently predict the development and lineage commitment of hematopoietic stem cells earlier than the beginning of any known developmental progress. There is also a deep-learning model named HE2RNA, which is able to predict the molecular phenotypes of tumors using hematoxylin & eosin (H&E)-stained histology slides alone.[10] Pengfei et al. applied machine learning in the development of a classifier to identify five molecular subtypes of breast cancer by reconstructing transcriptional classifications based on RNA-seq data.[11] These studies highlighted the possible further application of machine learning in the field of biomaterials research. Big data is the basis for success of a machine learning model.[12] Improvements in materiomics provide possible approaches by the accumulation of biomaterial-derived transcriptomic data in recent studies.[13] We hypothesize that machine learning could be used not only to identify physiological variations among cell types, but also to judge cellular functional changes induced by biomaterials. By learning from many sets of differentiated cellular whole-genome gene expression data, a machine learning model can be constructed to evaluate stem cell lineage fate based on global gene expression patterns. Hence, the output could be used to measure and compare the effects of biomaterials in regulating stem cell lineage fate.

In this study, we developed "Mesenchymal stem cell Differentiation Prediction (MeD-P)," an integrative package for evaluating biomaterial-induced human mesenchymal stem cells (hMSCs) lineage fate based on transcriptomic data. To obtain adequate data for machine learning, public RNA-seq datasets related to osteogenesis, chondrogenesis, and adipogenesis of hMSCs were collected and assigned to training datasets and testing datasets (**Figure 1**A). After batch effect adjustment and feature selection, the lineage-specific gene expression reference was constructed based on training datasets. And an evaluation model was implemented using machine learning algorithms that could predict lineage fate of hMSCs differentiation from gene expression patterns (Figure 1B). Then, several trial cases were implemented on representative biomaterials as examples. By comparing processed RNA-seq data with the gene expression reference, this model can compute lineage fate probabilities of hMSCs after incubation with the biomaterials (Figure 1C). The results proved that the model functioned reasonably well in evaluating hMSCs lineage fate accurately during the early stage.

2. Results

2.1. MeD-P Package Design

The MeD-P framework was designed to recognize cell lineage-specific features from public transcriptome data using machine learning for predicting biomaterial-induced stem cell lineage fate. The framework comprises three major parts: 1) Batch effect adjustment to remove unwanted data variances from different batches that arise from different cell sources and experimental conditions, that is, in training, testing, and predicting processes; 2) A lineage-specific gene expression reference for hMSCs that represents cell lineage-specific features was created for training the model; 3) Nine available machine learning methods were tested and the best one was selected as default in the prediction task. MeD-P takes RNA-seq data from biomaterial-induced hMSCs samples as input and predicts the cell differentiation state as probability of four possible cell lineages in this study, as illustrated in **Figure 2**.

2.2. Training, Validation, and Testing Dataset Allocation

We collected 12 public RNA-seq datasets encompassing chemically-induced tri-lineage differentiated human mesenchymal stem cells from 0 to 21 days of culture from two large-scale repositories GEO and ArrayExpress.[14–24] After filtering out unqualified samples using hierarchical cluster analysis (Figure S1, Supporting Information), we obtained a training dataset consisting of a total of 132 samples from 5 datasets (**Table 1**) and a testing set consisting a total of 96 samples from 7 datasets (**Table 2**), with labels in one of four distinct cell types including undifferentiated MSCs and three different cell lineages—osteogenic, chondrogenic, and adipogenic lineages. For the purpose of increasing the robustness of machine learning models against batch variances, we included RNA-seq data acquired using various hMSCs. The detailed information about the hMSCs used included 12 datasets that are listed in Data file S1, Supporting Information, including MSCs tissue origin, MSCs characterization information, MSCs culture medium, chemical components of differentiation induction medium, harvesting timepoints after differentiation induction, and biological replicates.

After that, the testing set was set aside and 70% of the training dataset was randomly selected as the actual training set with the remaining 30% as the validation set (**Table 3**). Briefly, according to stratified random sampling, 70% of samples in each cell type within the training dataset were randomly selected as the training set, while the remaining samples were collected as the validation set. Then the machine learning models can be iteratively trained and validated on these various splits.

2.3. Batch-Effect Adjustment Removes Undesired Batch Variances among Different Samples

Cell lineage-specific gene expression is the basis for learning and predicting differentiation states with this method. However, the batch variance that is unrelated to biological features could affect the feature learning and prediction. Therefore, we applied batch-effect adjustment on the training datasets before initiating learning of cell lineage-specific features. Circular hierarchical clustering on datasets before and after batch-effect adjustments revealed that samples were clustered

© 2023 Wiley-VCH GmbH

15214095, 2023, 19, Downloaded from https://onlinelibrary.wiley.com/doi/10.1002/adma.202210637 by Peking University Health, Wiley Online Library on [21/07/2023]. See the Terms and Conditions (https://onlinelibrary.wiley.com/terms-and-conditions) on Wiley Online Library for rules of use; OA articles are governed by the applicable Creative Commons License

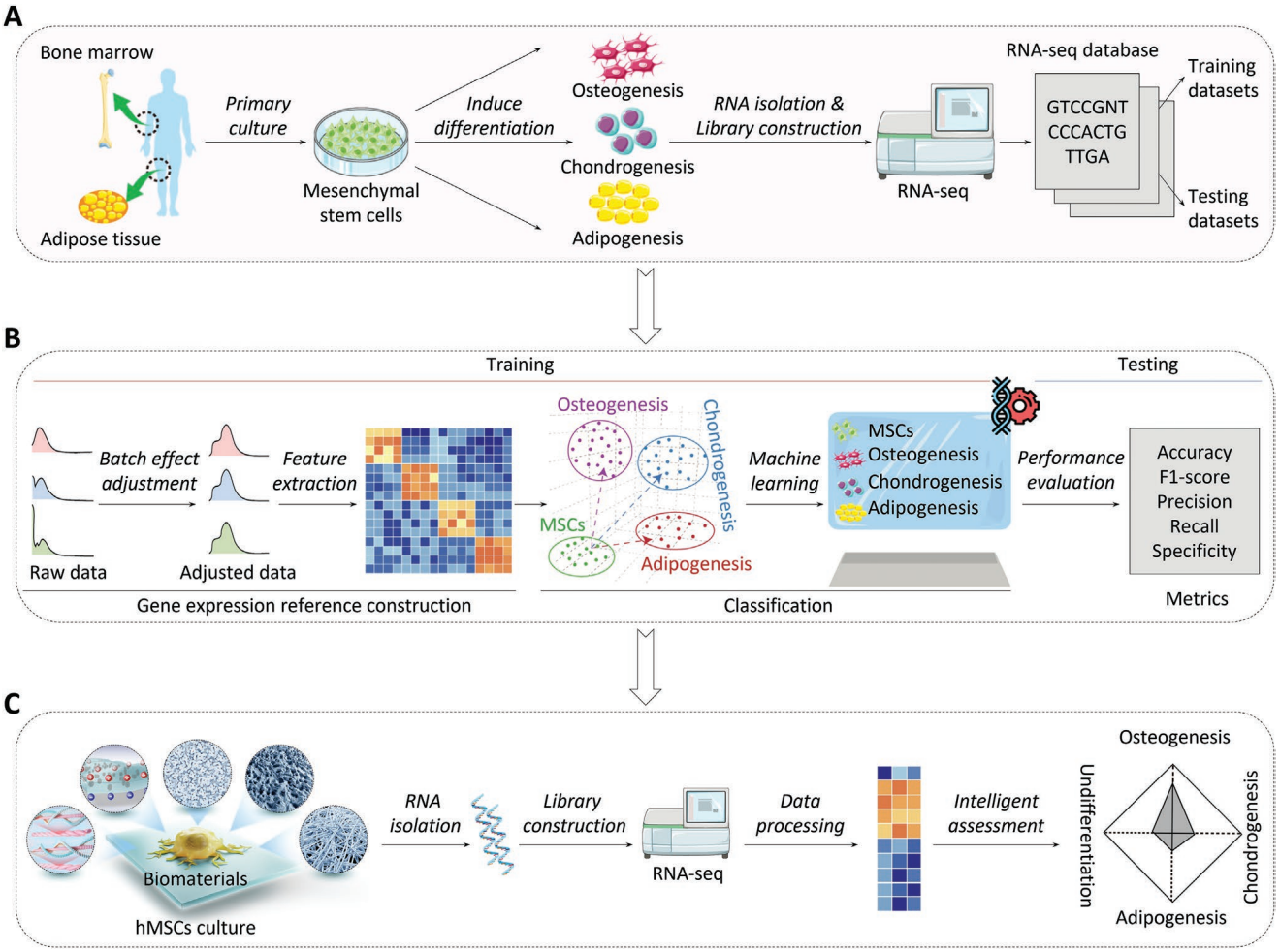

Figure 1. Overview of the workflow. A) We first collected RNA-seq datasets related to tri-lineage differentiation of human mesenchymal stem cells (hMSCs) from public databases and assigned them into training and testing datasets. B) Then bioinformatic analysis was performed on training datasets comprising quality control, batch effect adjustment and feature selection to obtain the regenerative gene expression reference for hMSCs. Based on this, the assessment model was implemented to predict hMSC lineage fate based on machine learning. Then the performance of the assessment model was evaluated on testing datasets. C) The assessment model was used to evaluate the regenerative potential of representative biomaterials. Briefly, hMSCs were cultured on biomaterials and harvested for RNA-seq. Processed RNA-seq data were loaded into the model and a report predicting tri-lineage differentiation probabilities was generated.

based on batches before adjustment, but not after adjustment (**Figure 3**A). The variation attributed to batch in the adjusted data was greatly reduced compared with that in the unadjusted data (Figure 3B). In addition, the adjustment also resulted in similar sample-level gene expression distribution among datasets (Figure 3C). The tSNE visualization of reduced dimensionality of transcriptome among datasets showed that samples were clustered according to batches and differentiation lineages before and after adjustment, respectively (Figure 3D). After adjustment, the normalized gene expression of housekeeping genes showed no differences among samples as exemplified by the following genes *CHMP2A*, *PPIA*, and *SNRPD3* (Figure S2A, Supporting Information), while there was higher expression of lineage-specific genes in the corresponding cell lineages compared to others, as exemplified by lineage-specific genes *OPN*, *ALPL*, *WNT2B* (for osteogenesis), *MATN3*, *SOX9*, *COL2A1* (for chondrogenesis), *PPARG*, *ADIPOQ*, and *CEBPA* (for adipogenesis) (Figure S2B–D, Supporting Information). These results thus suggest that batch-effect adjustment successfully removed undesired batch variances among different samples, while retaining the cell-type-specific differences.

2.4. Lineage-Specific Gene Expression Reference for hMSCs Differentiation

To predict the cell lineage fate, we selected only genes that represent the specificity of different cell lineages for model training.

Hence, we applied DESeq2 for feature genes selection by pair-wire comparison in four classes. For example, for osteogenesis-specific feature gene selection, we set the osteogenic samples as the experimental group, while the other three classes (chondrogenesis, adipogenesis, undifferentiated) were set as the control group respectively, followed by selection of three gene sets that are highly expressed in the experimental

© 2023 Wiley-VCH GmbH

15214095, 2023, 19, Downloaded from https://onlinelibrary.wiley.com/doi/10.1002/adma.202210637 by Peking University Health, Wiley Online Library on [21/07/2023]. See the Terms and Conditions (https://onlinelibrary.wiley.com/terms-and-conditions) on Wiley Online Library for rules of use; OA articles are governed by the applicable Creative Commons License

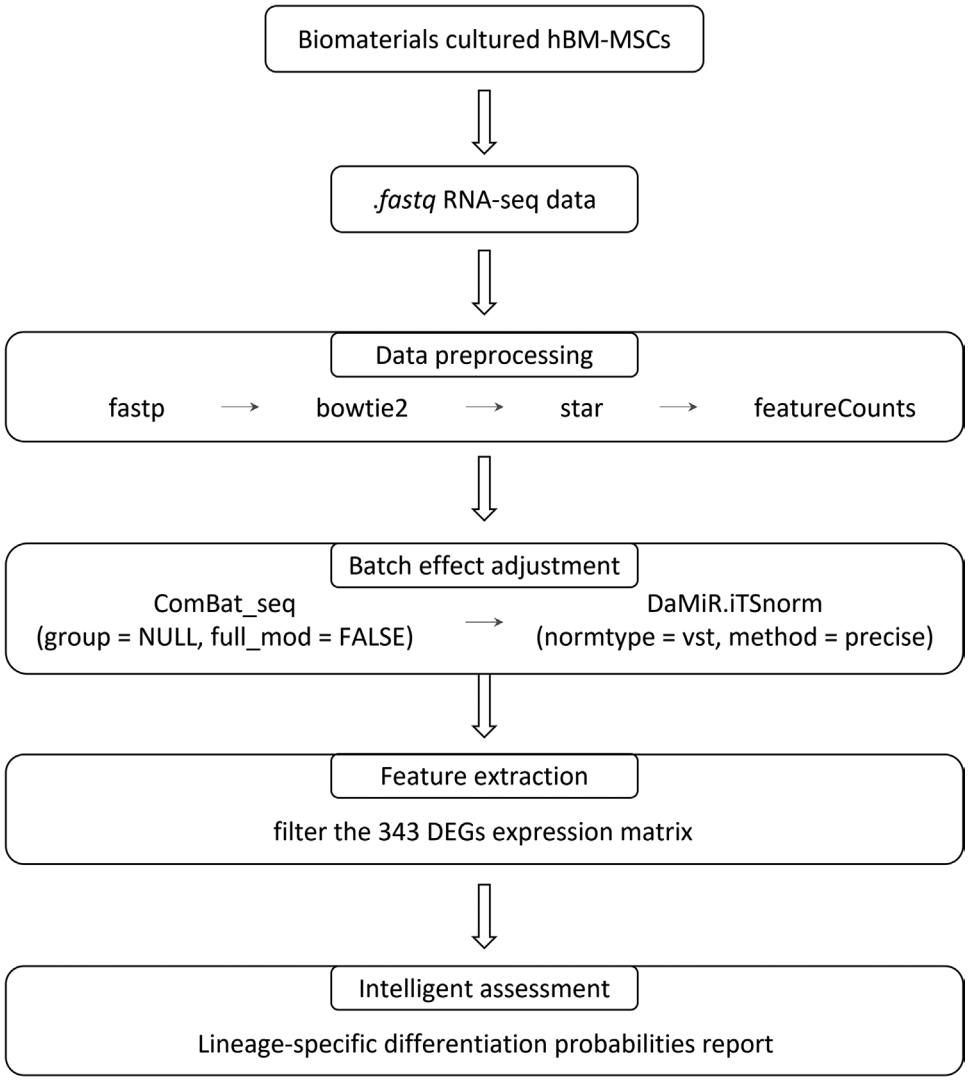

Figure 2. Utilization of package MeD-P. The *.fastq* file of RNA-seq data was initially pre-processed to obtain the gene expression count matrix using fastp, bowtie2, star, and featureCounts. Then ComBat_seq and DaMiR.iTSnorm was applied in adjusting the gene expression count distribution and normalizing the testing data to map with training data. The gene expression matrix of 343 DEGs was then extracted and loaded into the intelligent assessment model to obtain the differentiation scoring report for biomaterials cultured with hMSCs.

group, as compared with the three control groups respectively. Then we took the concatenation of the three gene sets as the highly expressed osteogenesis-specific gene list. After feature selection for the four classes, we collected the concatenation of the four characteristic gene lists as the overall feature genes. There included a total of 343 genes that were highly expressed

Table 1. Details of the training RNA-seq datasets after quality control.

Accession	Platform	Sample origin	Osteogenesis	Chondrogenesis	Adipogenesis	Undifferentiated	Reference
GSE113253	HiSeq 1500	BM-hMSC-TERT4[a)]	12	—	15	3	[14]
		AT-hMSC-TERT[b)]	8	—	10	2	
GSE109503	HiSeq 2500	hBM-MSC	—	11	—	3	[15]
GSE129036	NextSeq 500	hBM-MSC	17	—	—	4	[16]
GSE135775	HiSeq 4000	hBM-MSC	—	—	12	0	[17]
GSE161176	HiSeq 2500	hBM-MSC	—	26	—	9	[18]
SUM			37	37	37	21	

[a)]Telomerase-immortalized bone marrow-derived MSCs; [b)]Telomerase-immortalized adipose tissue-derived MSCs.

© 2023 Wiley-VCH GmbH

15214095, 2023, 19, Downloaded from https://onlinelibrary.wiley.com/doi/10.1002/adma.202210637 by Peking University Health, Wiley Online Library on [21/07/2023]. See the Terms and Conditions (https://onlinelibrary.wiley.com/terms-and-conditions) on Wiley Online Library for rules of use; OA articles are governed by the applicable Creative Commons License

15214095, 2023, 19, Downloaded from https://onlinelibrary.wiley.com/doi/10.1002/adma.202210637 by Peking University Health, Wiley Online Library on [21/07/2023]. See the Terms and Conditions (https://onlinelibrary.wiley.com/terms-and-conditions) on Wiley Online Library for rules of use; OA articles are governed by the applicable Creative Commons License

Table 2. Composition of public testing RNA-seq datasets after quality control.

Accession	Platform	Sample origin	Osteogenesis	Chondrogenesis	Adipogenesis	Undifferentiated	Reference
E-MTAB-6298	HiSeq 2500	hAD-MSC	12	—	12	11	[19]
GSE159138	HiSeq 2000	hAD-MSC	5	—	—	—	[20]
GSE159137	HiSeq 2000	hAD-MSC	—	—	—	5	[20]
E-MTAB-4879	HiSeq 2000	hBM-MSC	8	6	—	8	[21]
GSE114117	HiSeq X Ten	hBM-MSC	6	—	—	1	[22]
GSE166824	NextSeq 500	hBM-MSC	6	—	6	3	[23]
GSE174794	HiSeq X Ten	hBM-MSC	3	—	3	1	[24]
SUM			40	6	21	29	

in one of the four selected cell lineages. These genes with their corresponding expression levels were utilized as the lineage-specific gene expression reference for hMSCs differentiation. The expression profiles of selected genes are shown in the heatmap that displays cell lineage-specific gene expression patterns including some canonical marker genes (Figure 3E). Furthermore, the PCA analysis based on the selected gene expression profile showed a landscape with clustered samples and formation of three differentiation lineage pathways in the 3D PCA plot view (Figure 3F). Selected genes are listed in Data file S2, Supporting Information. These results suggest that selected genes were able to represent cell lineage-specific features, which could be used as a reference for training and predicting tasks.

2.5. Benchmarking of Machine Learning Models on Testing Datasets

We utilized a wide range of available machine learning methods, including Support Vector Machine with radial basis function kernel or linear kernel (SVM-R and SVM-L),[25] Random Forest (RF),[26] Gaussian Naive Bayes (GNB),[27] Linear Discriminant Analysis (LDA),[28] Logistic Regression (LR),[29] Multi-layer Perceptron (MLP),[30] RidgeClassifierCV (RidgeCV),[31] and k-nearest neighbors (kNN),[32] to train the prediction models. For each method, we optimized the parameters of the model through cross-validation based on the various splits of the training and validation sets. The trained models were applied on testing datasets to benchmark their prediction performance after removal of batch-effects (**Figure 4**A,B). The metadata of samples in the testing datasets are shown in Data file S3, Supporting Information, including hMSC sources, harvesting timepoints, and data accessions. Most of the chemically-induced samples (45 out of 78) were harvested on day 1–3.

We evaluated the nine established models (SVM-R, SVM-L, RF, GNB, LDA, LR, MLP, RidgeCV, kNN) based on accuracy, f1-score, precision, recall, and specificity, which are common performance evaluation metrics for machine learning models.[33] Among the five metrics, the f1-score and AUROC value are more comprehensive metrics for model performance evaluation relative to specificity and precision. For multi-class classification tasks like the task in this study, the overall f1-score and accuracy are the same value.[34] The results showed that the kNN model yielded the best performance on the basis of the overall evaluation, with the highest overall accuracy (90.63%), AUROC value (0.966), and per-class accuracy and f1-score (Figure 4C,D and **Figure 5**A,B). The kNN model also displayed quite high per-class precision, recall, specificity and overall

Table 3. The training, validation, and testing data set partitioning.

Accession	Data usage		Sample size [%]	Osteogenesis	Chondrogenesis	Adipogenesis	Undifferentiated
GSE113253	Modeling, cross-validation	Training set	93 (70%)	26 (70%)	26 (70%)	26 (70%)	15 (70%)
GSE109503							
GSE129036							
GSE135775		Validation set	39 (30%)	11 (30%)	11 (30%)	11 (30%)	6 (30%)
GSE161176							
			132 (100%)	**37 (100%)**	**37 (100%)**	**37 (100%)**	**21 (100%)**
E-MTAB-6298	Benchmarking	Testing set	**96 (100%)**	**40 (100%)**	**6 (100%)**	**21 (100%)**	**29 (100%)**
GSE159138							
GSE159137							
E-MTAB-4879							
GSE114117							
GSE166824							
GSE174794							

 © 2023 Wiley-VCH GmbH

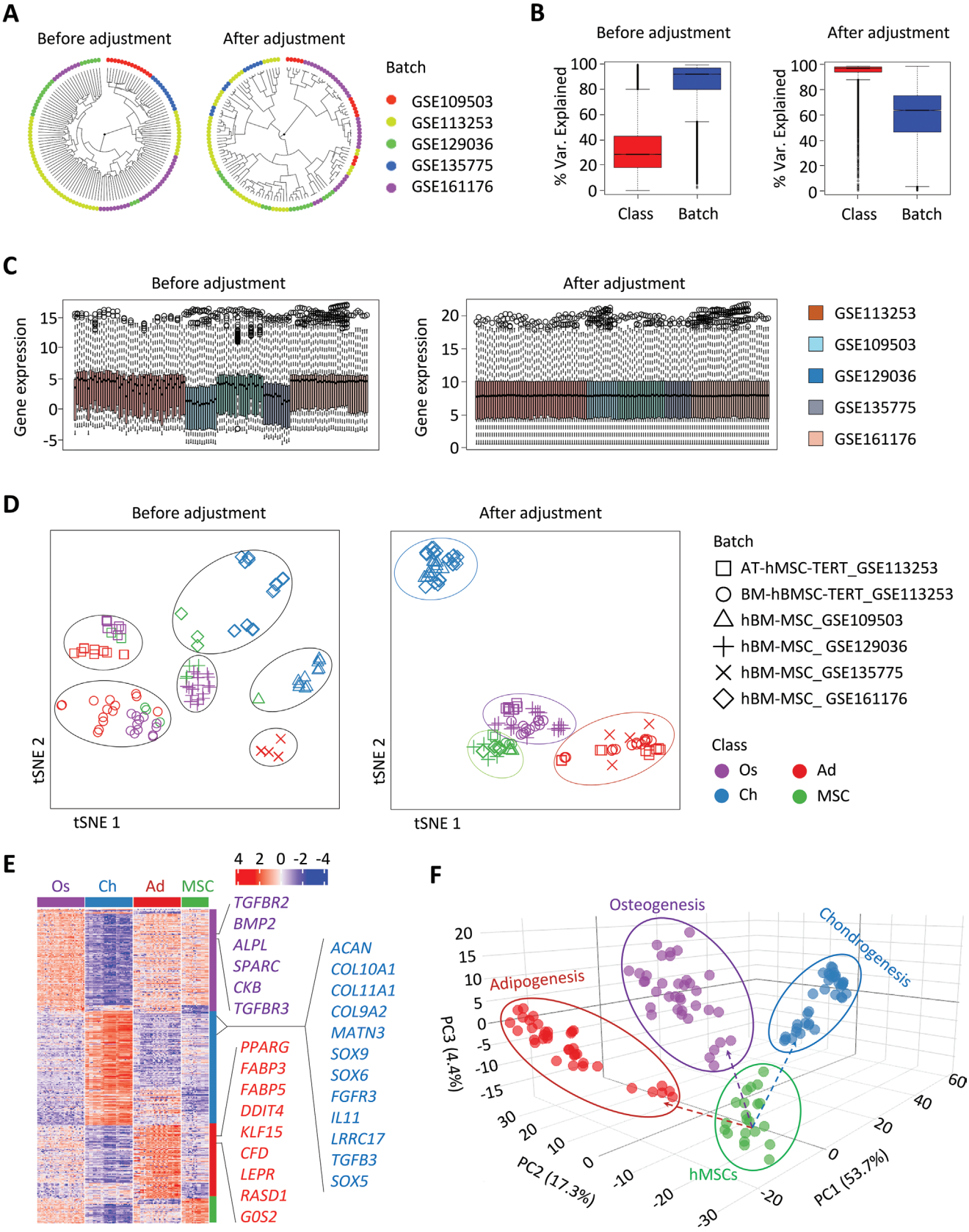

Figure 3. The regenerative gene expression reference for hMSCs was constructed. A) The circular dendrograms revealed that hierarchical clustering did not match original batches in the adjusted data (right) better compared with the unadjusted data (left). The samples are colored by batch. B) In the

© 2023 Wiley-VCH GmbH

15214095, 2023, 19, Downloaded from https://onlinelibrary.wiley.com/doi/10.1002/adma.202210637 by Peking University Health, Wiley Online Library on [21/07/2023]. See the Terms and Conditions (https://onlinelibrary.wiley.com/terms-and-conditions) on Wiley Online Library for rules of use; OA articles are governed by the applicable Creative Commons License

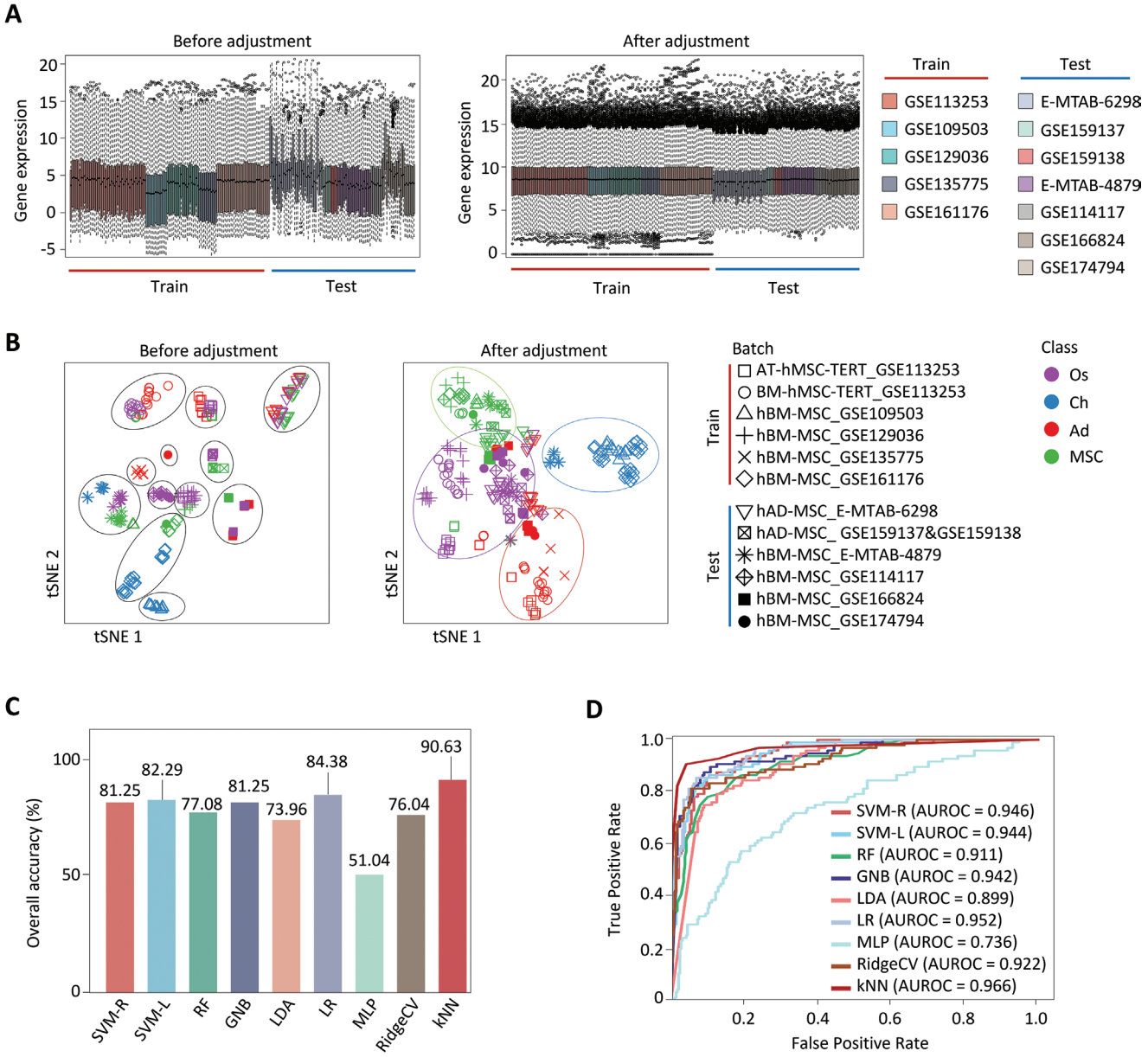

Figure 4. Data adjustment effectively reduced batch variation in testing datasets. A) The boxplots showed sample-level gene expression distribution in independent testing datasets together with the five training datasets before (left) and after (right) data adjustment. B) The tSNE plots revealed that samples were clustered according to original batches in the unadjusted data (left). Within the adjusted data (right), samples were clustered by cell lineages. Different cell lineages and batches in samples are represented by different colors and shapes respectively. C) The overall accuracy of nine models in benchmarking the testing datasets. D) The micro-average ROC curves of nine models. Abbreviations: ROC, receiver operating characteristic; AUROC, area under ROC curve.

specificity (Figure 5C–F). Although several models had a higher overall specificity, per-class specificity, or per-class precision than kNN (Figure 5C–F), they did not manifest advantages in the overall accuracy (f1-score) and AUROC values (Figure 4C,D). Hence, the kNN model was selected as the default model for MeD-P.

adjusted data (right), batch variation was greatly reduced compared with that in the unadjusted data (left). C) The boxplot showed that sample-level gene expression value distribution across five batches were similar in the adjusted data (right), while there was clear distributional difference across batches before batch effect adjustment was carried out (left). D) The tSNE plots revealed that samples were clustered according to original batches in the unadjusted data (left). While in the adjusted data (right), samples were clustered by cell lineages. E) Heatmap showing the characteristic gene expression profiles of the reference, containing canonical marker genes. F) 3D PCA plot visualized the relative spatial distance among the four clusters of samples. Different cell lineages and batches in the samples are represented by different colors and shapes respectively. Abbreviations: Ad, Adipogenesis; Ch, Chondrogenesis; MSC, Mesenchymal stem cells; Os, Osteogenesis.

© 2023 Wiley-VCH GmbH

15214095, 2023, 19, Downloaded from https://onlinelibrary.wiley.com/doi/10.1002/adma.202210637 by Peking University Health, Wiley Online Library on [21/07/2023]. See the Terms and Conditions (https://onlinelibrary.wiley.com/terms-and-conditions) on Wiley Online Library for rules of use; OA articles are governed by the applicable Creative Commons License

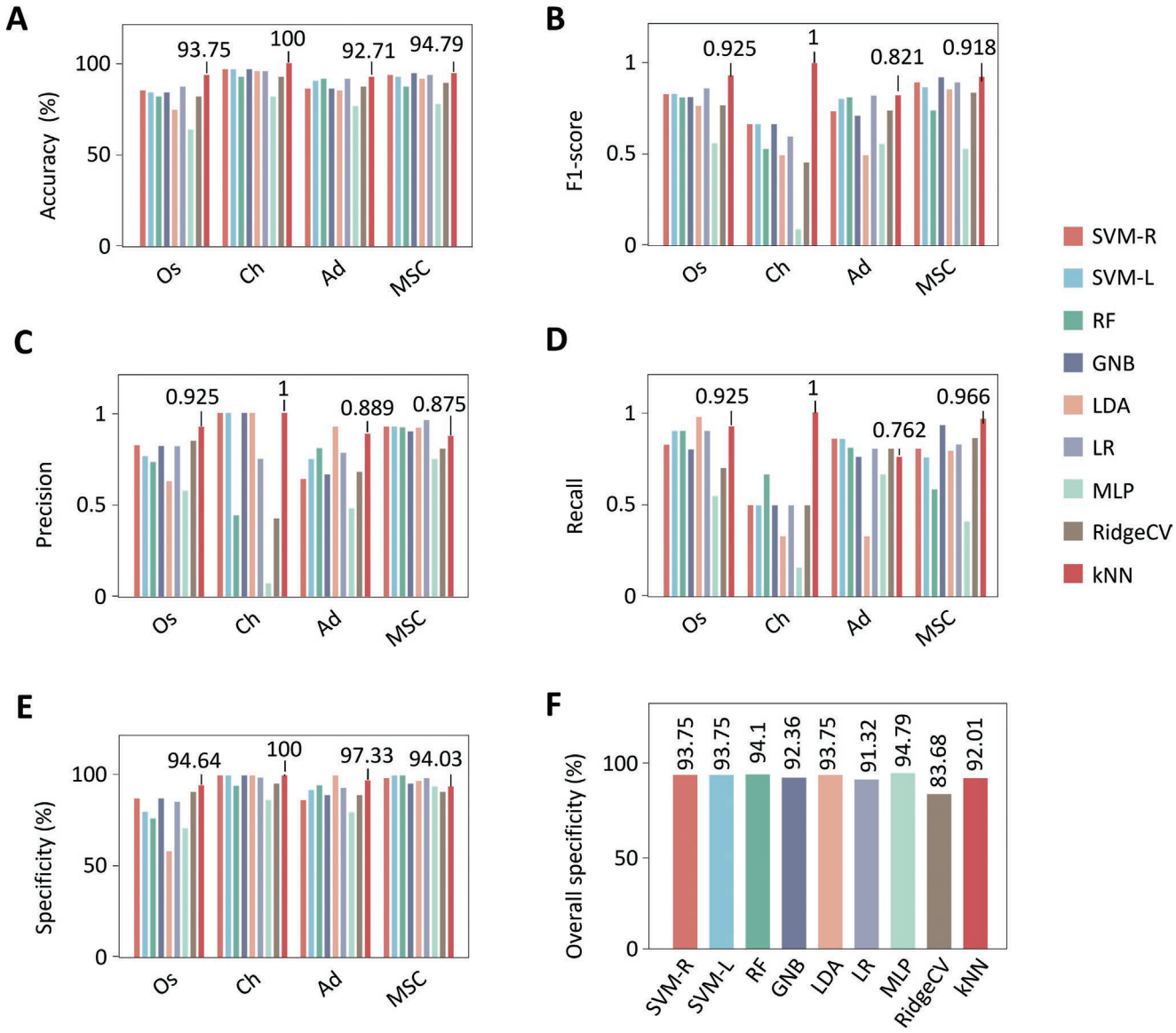

Figure 5. Performance comparison of nine machine-learning models in benchmarking public testing datasets. A) The per-class accuracy on testing datasets among nine machine-learning models. B) The per-class f1-score on testing datasets among nine machine-learning models. C) The per-class precision on testing datasets among nine machine-learning models. D) The per-class recall on testing datasets among nine machine-learning models. E) The per-class specificity on testing datasets among nine machine-learning models. F) The overall specificity on testing datasets among nine machine-learning models.

We further examined the prediction ability of the kNN model on different cell lineages of the testing datasets and found that the precision and recall were both 0.925 on average for 40 osteogenesis samples (**Figure 6**A). A small portion of the osteogenesis samples were mis-predicted as adipogenesis samples and undifferentiated MSCs samples (Figure 6B,C). The prediction on adipogenesis samples had the lowest recall (0.762) compared to other cell types, with only 3 and 2 samples being mis-predicted as undifferentiated MSCs and osteogenesis samples, respectively. The prediction accuracy on chondrogenesis and undifferentiated MSCs samples were generally high with values of 100% and 94.79% respectively. Consistently, the ROC curves showed that the chondrogenesis samples and undifferentiated MSCs samples have the highest AUROC scores (1.000 and 0.993, respectively) while the adipogenesis samples had the lowest AUROC score (0.897). Overall, the prediction of the kNN model had the highest AUROC score (0.966) among all models (Figure 6D).

2.6. Model Trained on Selected Gene Expression Reference Outperforms Those Trained on Canonical Marker Genes and the All-Gene-Set

When generating the training model, we questioned whether the selected lineage-specific gene expression reference was

© 2023 Wiley-VCH GmbH

15214095, 2023, 19, Downloaded from https://onlinelibrary.wiley.com/doi/10.1002/adma.202210637 by Peking University Health, Wiley Online Library on [21/07/2023]. See the Terms and Conditions (https://onlinelibrary.wiley.com/terms-and-conditions) on Wiley Online Library for rules of use; OA articles are governed by the applicable Creative Commons License

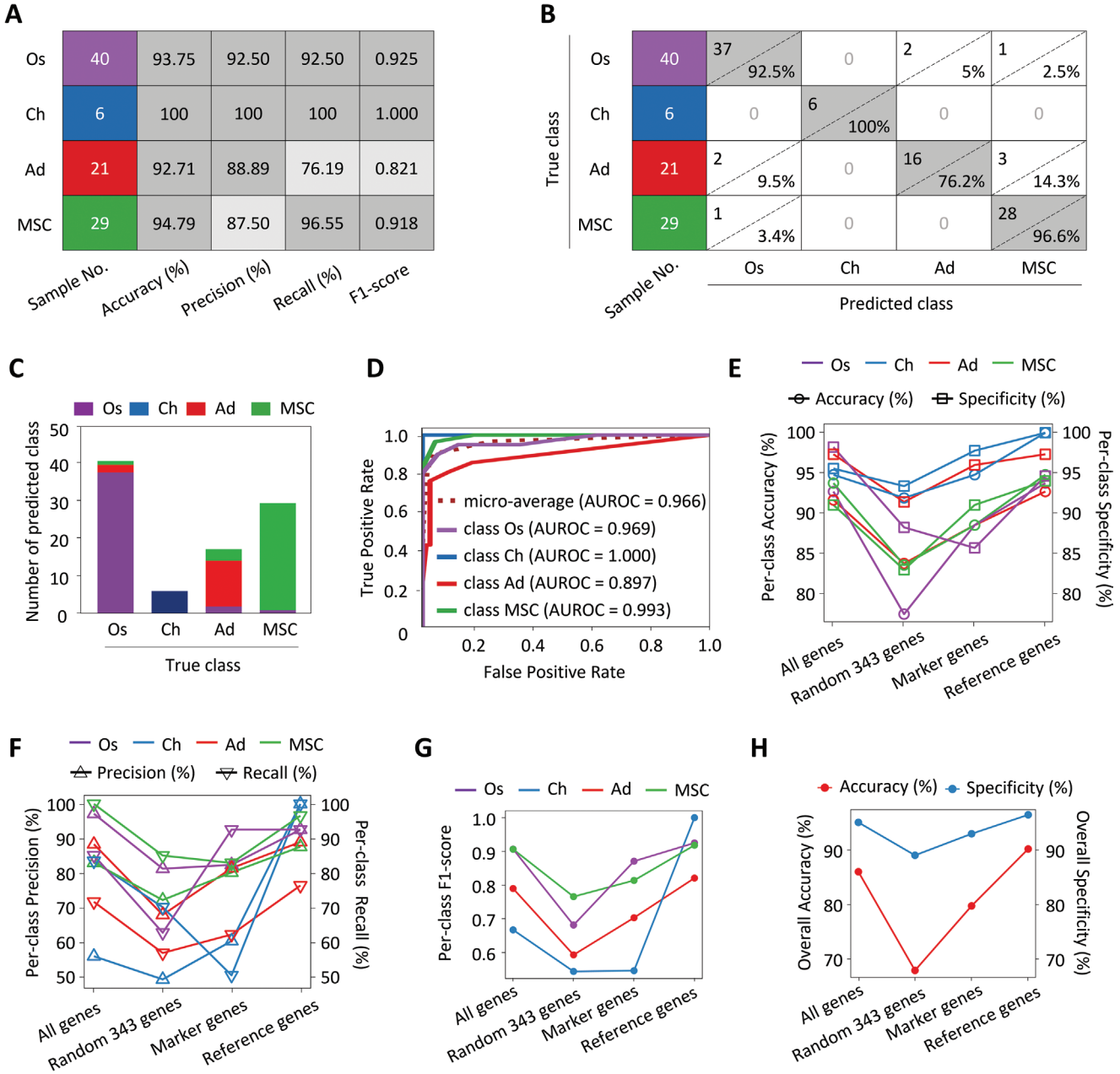

Figure 6. Machine learning performed well in hMSCs lineage fate assessment. A) The classification report showed the accuracy, precision, recall, and f1-score of the model on four classes with different number of samples. B) The classification prediction error report showed the numbers of correctly and wrongly predicted samples. C) The confusion matrix showed the detailed sample composition of predicted classes in the actual classes. D) The ROC curve and AUROC values showed that the model obtained high performance in generalization ability. E) The linechart showed that the reference genes obtained much higher per-class accuracy and specificity compared with random 343 genes and canonical marker genes, but were slightly higher than the all gene-set. F) The linechart showed that the reference genes obtained higher per-class precision and recall compared with random 343 genes, marker genes and all genes. G) The linechart showed that the reference genes obtained the highest per-class f1-score compared with random 343 genes, marker genes and all genes. H) The linechart showed that the reference genes obtained the highest overall accuracy and specificity compared with random 343 genes, marker genes, and all genes.

better than known canonical lineage-specific marker genes as training features. To address this issue, we generated the training model on canonical lineage-specific marker genes (Table S1, Supporting Information) on the same training samples and did prediction on the same testing datasets with the same machine learning methods and procedures. In addition, we also tested the models trained on randomly-selected gene sets with the same number of genes as the selected gene reference, as well as the model trained on all genes that passed the quality control. Comparisons of these models on the testing datasets showed that the model trained on the selected gene expression reference had higher per-class accuracy, specificity,

© 2023 Wiley-VCH GmbH

15214095, 2023, 19, Downloaded from https://onlinelibrary.wiley.com/doi/10.1002/adma.202210637 by Peking University Health, Wiley Online Library on [21/07/2023]. See the Terms and Conditions (https://onlinelibrary.wiley.com/terms-and-conditions) on Wiley Online Library for rules of use; OA articles are governed by the applicable Creative Commons License

Table 4. Reference genes performed well in hMSCs lineage fate assessment compared with other gene sets.

		All genes	Random 343 genes	Marker genes	Reference genes
Per-class accuracy [%]	Os	92.70833	77.50577	88.54167	93.75
	Ch	94.79167	91.91291	94.79167	100
	Ad	91.66667	83.78668	88.54167	92.70833
	MSC	93.75	83.59916	88.54167	94.79167
Per-class F1-score	Os	0.906667	0.681031	0.870588	0.925
	Ch	0.666667	0.54313	0.545455	1
	Ad	0.789474	0.59244	0.702703	0.820513
	MSC	0.90625	0.765411	0.813559	0.918033
Per-class precision [%]	Os	97.14286	81.10073	82.22222	92.5
	Ch	55.55556	48.80086	60	100
	Ad	88.23529	67.64129	81.25	88.88889
	MSC	82.85714	71.9538	80	87.5
Per-class recall [%]	Os	85	62.432	92.5	92.5
	Ch	83.33333	69.86482	50	100
	Ad	71.42857	56.5117	61.90476	76.19048
	MSC	100	84.94492	82.75862	96.55172
Per-class specificity [%]	Os	98.21429	88.27275	85.71429	94.64286
	Ch	95.55556	93.38279	97.77778	100
	Ad	97.33333	91.42367	96	97.33333
	MSC	91.04478	83.01667	91.04478	94.02985
Overall accuracy [%]		86.45833	68.40226	80.20833	90.625
Overall specificity [%]		95.48611	89.46742	93.40278	96.875

precision, recall, and f1-score, as compared to those trained on canonical marker genes, randomly-selected gene sets, and the allgene-set (Figure 6E–G and **Table 4**). The reference gene set also had the overall highest accuracy and specificity (Figure 6H).

Furthermore, because day 7 is a common timepoint for evaluating biomaterials-induced MSCs differentiation,[35] we have added the comparison between canonical marker genes and reference genes-supported MeD-P using day 7 samples, from both the public testing datasets and tri-lineage differentiation experiments in our own laboratory. The results demonstrated that reference genes-supported MeD-P had a higher overall accuracy than canonical marker genes in benchmarking day 7 samples, especially for the undifferentiated samples (Figure S3A,B, Supporting Information).

These results thus demonstrate the potential and efficiency of the selected gene expression reference as the training features for the prediction model.

2.7. MeD-P Provides Robust, Accurate, and Quick Predictions on Varied Biomaterial-Induced hMSCs Lineage Fate

For evaluation, human bone marrow-derived mesenchymal stem cells (hBM-MSCs) were cultured on representative biomaterials and harvested for RNA-seq after 7 days. Processed RNA-seq data were loaded into MeD-P, and a report on tri-lineage differentiation probabilities was generated (**Figure 7**A).

The 3D-printed beta-tricalcium phosphate (β-TCP) scaffolds had a porous network structure with high specific surface area, exhibiting ability to control the release of bioactive ions (Figure S4A–E, Supporting Information). The electrospun poly-L-lactic acid (PLLA) nanofibrous membranes had uniform nanofibers, which displayed biomimetic nano-topography similar to that of the extracellular matrix in the randomly-oriented (RD) group and were arranged in parallel in the aligned (AL) group (Figure S5A,B, Supporting Information). Sandblasting with large grit and acid-etching (SLA)-treated Ti-6Al-4V substrates had a rough morphology mimicking the surface texture of dental implants (Figure S6A–D, Supporting Information). These biomaterials are widely investigated in regenerative medicine and have displayed much potential in stem cell osteogenic regulation.[36] The $BaTiO_3$ nanoparticles (BTO NPs)/poly(vinylidene fluoridetrifluoroethylene) (P(VDF-TrFE)) nanocomposite membranes displayed stable electroactivity after polarization (Figure S7A–E, Supporting Information). The L-phenylalanine (LH) and the D-phenylalanine (DH) hydrogel matrices exhibited a helical 3D network structure in nanoscale, and the nanofibers had the characteristics of left-handed and right-handed ultrachiral assembly properties, respectively (Figure S8A,B, Supporting Information). Our previous researches have found that polarized BTO NPs/P(VDF-TrFE) nanocomposite membranes and L-phenylalanine hydrogel matrices could induce the osteogenesis of MSCs, and that D-phenylalanine hydrogel matrices had inductive potential in adipogenic differentiation of MSCs.[35a,b]

hBM-MSCs used in the biomaterials-related experiments were characterized by cell surface antigen expression profile and validation of tri-lineage differentiation potential as shown in Figure S9, Supporting Information. It can be seen from Figure S9A, Supporting Information, that hBM-MSCs at passage 3 exhibited spindle-shaped morphology. As shown in Figure S9B, Supporting Information, there were 99.83%, 98.90%, 97.71%, 99.86%, 99.68% of the hBM-MSCs population expressing positive MSC antigen markers CD29 (v), CD166 (vi), CD105 (vii), CD73 (viii), and CD44 (ix), respectively. While less than 4.00% of the hBM-MSCs population expressed negative MSC antigen markers CD14 (x), CD45 (xi), CD34 (xii), CD11b (xiii), and HLA-DR (xiv). The tri-lineage differentiation potential of hBM-MSCs were validated by Alizarin Red S, alkaline phosphatase (for osteogenesis), Alcian Blue (for chondrogenesis), and Oil Red O (for adipogenesis) staining after 14 or 21 days of induction, as demonstrated in Figure S9C–E, Supporting Information. The quantitative real-time PCR also demonstrated significant upregulation of lineage-specific early marker genes in tri-lineage differentiated hBM-MSCs (Figure S9F, Supporting Information).

Then we respectively collected RNA-seq data of hBM-MSCs and processed these using the MeD-P package after 7 days of culture on 3D-printed β-TCP scaffolds, electrospun PLLA nanofibrous membranes, SLA-treated Ti-6Al-4V substrates, BTO NPs/P(VDF-TrFE) nanocomposite membranes, and phenylalanine hydrogel matrices. The hBM-MSCs were also cultured in normal culture medium for 7 days and collected as blank control. The assessment report of MeD-P showed that the β-TCP scaffolds yielded the highest probability in inducing osteogenesis of hBM-MSCs (Figure 7B,C), which was validated

© 2023 Wiley-VCH GmbH

15214095, 2023, 19, Downloaded from https://onlinelibrary.wiley.com/doi/10.1002/adma.202210637 by Peking University Health, Wiley Online Library on [21/07/2023]. See the Terms and Conditions (https://onlinelibrary.wiley.com/terms-and-conditions) on Wiley Online Library for rules of use; OA articles are governed by the applicable Creative Commons License

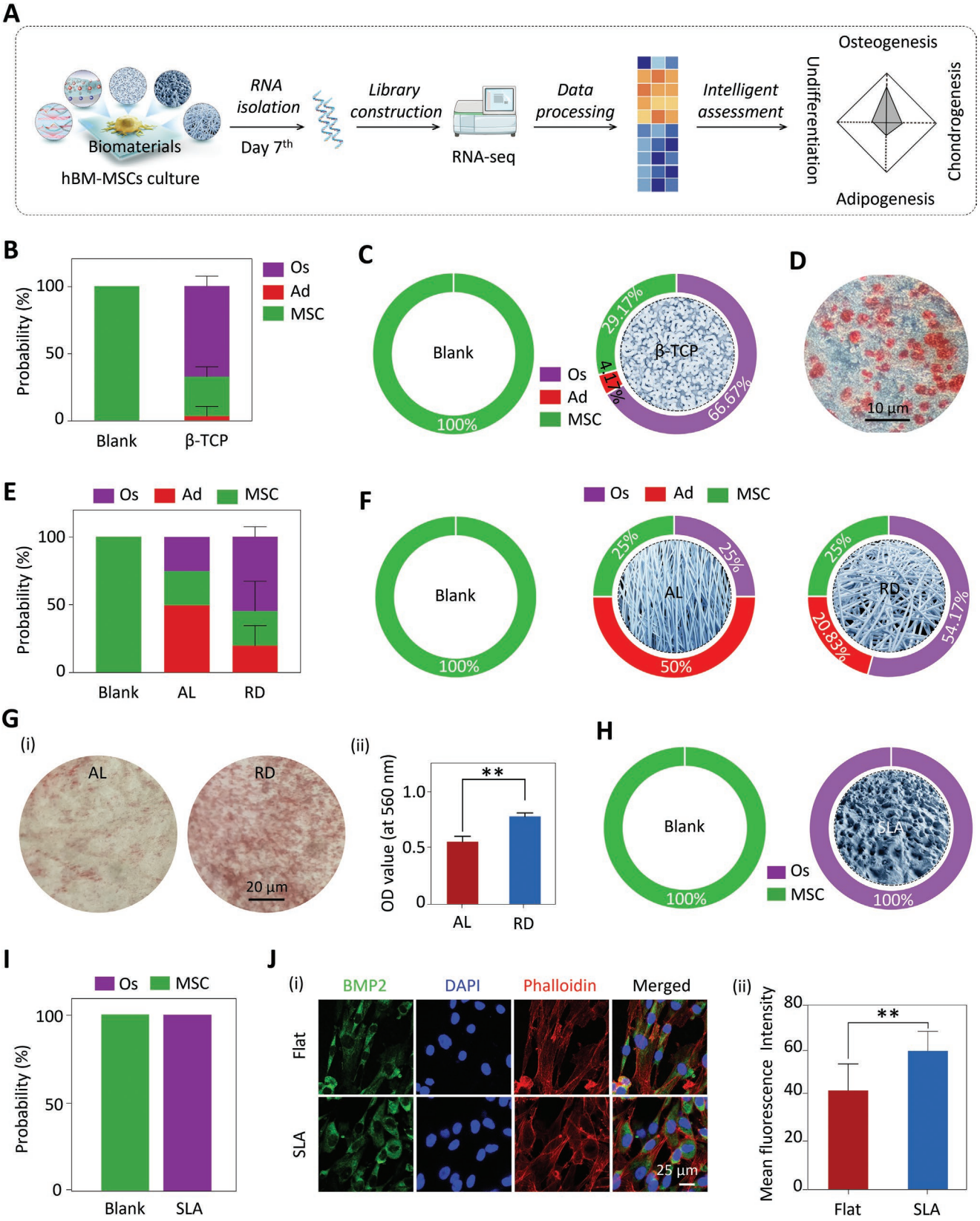

Figure 7. MeD-P provided accurate predictions of representative biomaterial-induced hMSCs lineage fate. A) The scheme of model application. MeD-P was used to evaluate the regenerative potential of representative biomaterials. Briefly, hBM-MSCs were cultured on biomaterials and harvested for RNA-seq after 7 days of culture. Processed RNA-seq data were loaded into the model and generated a report predicting tri-lineage differentiation

© 2023 Wiley-VCH GmbH

15214095, 2023, 19, Downloaded from https://onlinelibrary.wiley.com/doi/10.1002/adma.202210637 by Peking University Health, Wiley Online Library on [21/07/2023]. See the Terms and Conditions (https://onlinelibrary.wiley.com/terms-and-conditions) on Wiley Online Library for rules of use; OA articles are governed by the applicable Creative Commons License

15214095, 2023, 19, Downloaded from https://onlinelibrary.wiley.com/doi/10.1002/adma.202210637 by Peking University Health, Wiley Online Library on [21/07/2023]. See the Terms and Conditions (https://onlinelibrary.wiley.com/terms-and-conditions) on Wiley Online Library for rules of use; OA articles are governed by the applicable Creative Commons License

by Alizarin Red S (ARS) staining on day 21 (Figure 7D). The differentiation scores showed that after incubation with β-TCP scaffolds, hBM-MSCs yielded higher osteogenic differentiation scores compared with the blank control (Figure S4F, Supporting Information). Upon examining the expression levels of several osteogenic marker genes such as *ALPL*, *RUNX2*, and *COL1A2*, it was noticed that the expression of these genes was upregulated after culturing cells on the β-TCP scaffolds for 7 days, which was comparable with the osteogenic induction medium (Figure S4G, Supporting Information).

MeD-P predicted the highest probability of adipogenesis for hBM-MSCs cultured in the AL group, and the highest probability of osteogenensis for hBM-MSCs cultured in the RD group (Figure 7E,F). The osteogenic differentiation of hBM-MSCs cultured in the RD group was validated by ARS staining on the 21st day of cell culture (Figure 7G). The microscopy images and relative quantification of stained mineralized nodules demonstrated that the RD group had stronger osteo-inductive capacity than the AL group. Additionally, hBM-MSCs cultured in the RD group also yielded a much higher osteogenic differentiation score than the AL group (Figure S5C, Supporting Information). Examining the gene expression profiles revealed that several adipogenic marker genes had higher expression levels in the AL group, while several osteogenic marker genes had higher expression levels in the RD group on the 7th day of cell culture (Figure S5D, Supporting Information), which was consistent with the MeD-P prediction. Similarly, MeD-P predicted that the SLA-treated Ti-6Al-4V substrates strongly induced osteogenic differentiation of hBM-MSCs with 100% probability (Figure 7H,I), which was validated by the upregulated expression of the pro-osteogenic growth factor BMP2 on the 3rd day of culture (Figure 7J). The osteo-inductive capacity of SLA-treated Ti-6Al-4V substrates was also validated by its increased osteogenic differentiation score, as well as expression of several osteogenic marker genes such as *ALPL*, *BMP2*, and *OPTN* on the 7th day (Figure S6E,F, Supporting Information).

Reports of MeD-P showed that the polarized BTO NPs/P(VDF-TrFE) nanocomposite membranes had a prevailing osteogenic induction potential (**Figure 8**A,B), which was verified by ARS staining on the 21st day of cell culture and upregulated expression of the pro-osteogenic growth factor BMP2 on the 3rd day of cell culture (Figure 8C,D). It was also shown in the MeD-P predicted reports that the L-phenylalanine hydrogel could induce the osteogenesis of hBM-MSCs, while the D-phenylalanine hydrogel obviously promoted adipogenesis (Figure 8E,F). The chirality-dependent lineage specification of mesenchymal stem cells was validated by alkaline phosphatase (ALP) staining and Oil Red O staining after incubation of hBM-MSCs for 14 days in chiral phenylalanine hydrogels (Figure 8G), which were consistent with our published research results.[35b] The differentiation scores and gene expression patterns of hBM-MSCs on the 7th day of culture was consistent with the MeD-P predictions for both the piezoelectric BTO NPs/P(VDF-TrFE) membranes (Figure S7F,G, Supporting Information) and chiral hydrogel matrices (Figure S8C,D, Supporting Information).

In this section, MeD-P was applied for assessing the function of biomaterials in regulating stem cell lineage fate, demonstrating its excellent performance in predicting biomaterial-induced hMSCs lineage fate accurately at as early as the 7th day of culture. Taken together, these results thus suggest that MeD-P provides a robust, accurate, and quick prediction of biomaterial-induced hMSCs lineage fate.

3. Discussion

Biological performance evaluation is a key process in regenerative biomaterials research.[37] In particular, the ability to regulate stem cell lineage fate is crucial to the clinical translation potential of newly-developed biomaterials.[3b,38] However, current laboratory techniques are limited with regards to stem cell lineage fate characterization. For example, the validation of MSCs differentiation by conventional staining methods such as Alizarin Red S staining, Oil Red O staining, and Alcian Blue staining does not guarantee data reproducibility. Alternatively, MeD-P is able to eliminate batch differences of MSCs-related RNA-seq data from different laboratories or batches to a certain extent, thus providing a way to improve the reproducibility of MSCs-related data. Moreover, the staining methods are rather time-consuming, and usually take several days to determine the lineage fate of MSCs differentiation, for example, 21 days for ARS staining to observe mineralized nodules (osteogenic differentiation).[39] In our study, the default model in MeD-P can accurately predict the lineage fate direction on 90.63% of testing samples, most of which (45 out of 78) were harvested after 1–3 days of induction, as shown in Data file S3, Supporting Information, which means significant time-savings for evaluation of stem cell lineage fate prediction. For characterizing MSC-biomaterial interactions, day 7 is a common timepoint for early differentiation evaluation.[35] In this study, we chose to harvest RNA-seq samples on day 7 for representative biomaterials evaluation.

Additionally, common molecular labeling techniques can be restricted by limited current understanding of canonical biomarkers of MSCs differentiated cell types, and may also be affected by many experimental variables, such as laboratory equipment and testing agent.[6c,8,11] Hence, comparison of regenerative potential of different biomaterials based on current approaches might not be easily carried out. It is rather

probabilities. B,C) The differentiation probabilities obtained from MeD-P predicted the osteo-inductive function of β-TCP scaffolds. D) Representative ARS staining microscopy images of hBM-MSCs after 21 days of cultivation on β-TCP scaffolds. E,F) The differentiation probabilities obtained from MeD-P predicted the adipo-inductive and osteo-inductive functions of aligned (AL) and randomly-oriented (RD) PLLA nanofibrous membranes respectively. G) Representative i) ARS staining microscopy images and ii) relative ARS quantification of hBM-MSCs after 21 days of cultivation on PLLA nanofibrous membranes. H,I) The differentiation probabilities obtained from MeD-P yielded strong osteo-inductive function of the SLA-treated Ti-6Al-4V alloy substrates. J) Representative i) immunofluorescence microscopy images and ii) mean fluorescence intensity of BMP2 protein expression in hBM-MSCs after 3 days of incubation on Ti-6Al-4V alloy substrates. Error bars represent standard error of the mean, $n = 3$. $^{**}p < 0.01$, indicating a statistically significant difference.

 © 2023 Wiley-VCH GmbH

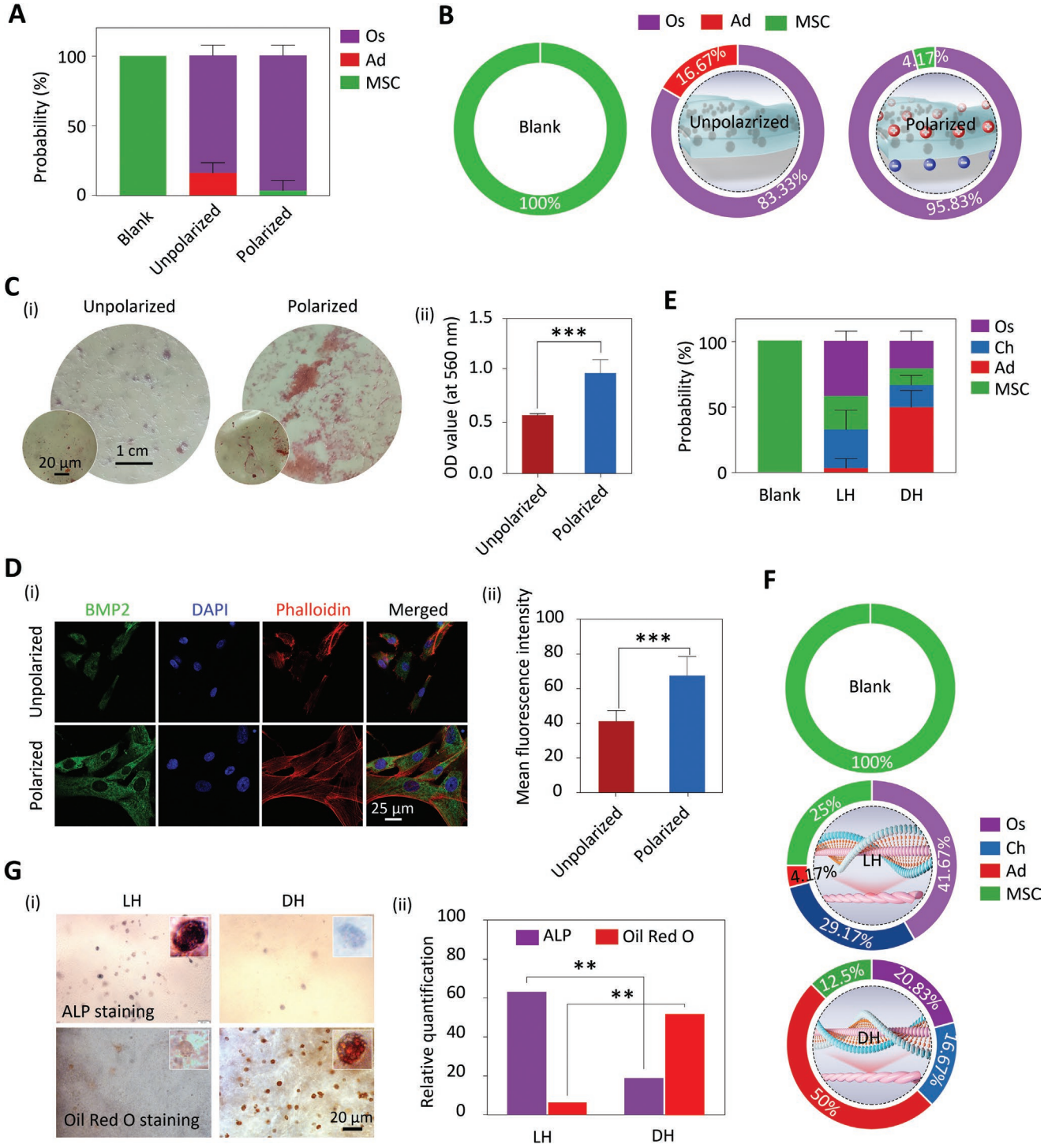

Figure 8. MeD-P predicted the mesenchymal stem cell lineage fate regulated by electroactivity and chirality accurately. A,B) The differentiation probabilities obtained from MeD-P predicted the osteo-inductive function of unpolarized (UP) and polarized (P) BTO NPs/P(VDF-TrFE) membranes. C) Representative i) ARS staining microscopy images and ii) relative ARS quantification of hBM-MSCs after 21 days of incubation on BTO NPs/P(VDF-TrFE) membranes. D) Representative i) immunofluorescence microscopy images and ii) mean fluorescence intensity of BMP2 protein expression in hBM-MSCs after 3 days of incubation on BTO NPs/P(VDF-TrFE) membranes. E,F) The differentiation probabilities obtained from MeD-P predicted the osteo-inductive function of L-phenylalanine chiral hydrogel (LH) matrices and adipo-inductive function of D-phenylalanine chiral hydrogel (DH) matrices after 7 days of cultivation. G) ALP and lipid droplet i) staining microscopy images and ii) the relative quantification of hBM-MSCs after 14 days of incubation, indicating that the LH matrices significantly enhanced the osteogenic lineage commitment, and that the DH matrices significantly promoted adipogenic lineage commitment. Error bars represent standard error of the mean, $n = 3$. $^{**}p < 0.01$, $^{***}p < 0.001$, indicating a statistically significant difference.

© 2023 Wiley-VCH GmbH

15214095, 2023, 19, Downloaded from https://onlinelibrary.wiley.com/doi/10.1002/adma.202210637 by Peking University Health, Wiley Online Library on [21/07/2023]. See the Terms and Conditions (https://onlinelibrary.wiley.com/terms-and-conditions) on Wiley Online Library for rules of use; OA articles are governed by the applicable Creative Commons License

challenging to precisely identify the physicochemical factors of biomaterials that can induce lineage-specific MSCs differentiation, which thus limits the development of related therapeutic applications.[40] Through data adjustment in MeD-P, the batch variation effect between the testing dataset and the training gene expression reference can be alleviated, which means that MeD-P is capable of comparing RNA-seq data generated by various types of biomaterials from different laboratories. The inductive function of biomaterials on hMSCs lineage fate is evaluated based on three aspects: osteogenic, chondrogenic, and adipogenic differentiation. Compared with conventional methods, the inductive potential of biomaterials in regulating stem cell lineage fate can be more intuitively and comprehensively evaluated and compared by this artificial intelligence-based assessment model.

In this study, we explored the strategy of using transcriptome as the basis for stem cell lineage identification, and constructed an intelligent model for the assessment of hMSCs lineage fate based on big data and machine learning. By comparing the transcriptome to be tested with the gene expression reference of hMSCs tri-lineage differentiation, the performance of biomaterials in regulating hMSCs differentiation toward the osteogenic, chondrogenic, and adipogenic lineages can be accurately evaluated by this artificial intelligence-based assessment model. As observed, our data-driven machine learning model is capable of deciphering stem cell lineage fate independent of prior knowledge because the selected lineage-specific gene expression reference outperforms known canonical lineage-specific marker genes as the training features.

As a novel technique for evaluating stem cell lineage fate, the artificial intelligence-based assessment model we proposed was validated to be accurate, robust, practical and batch-independent in estimating the inductive potential of biomaterials in regulating lineage-specific differentiation of MSCs. Assessment reports generated by MeD-P deduced that 3D-printed β-TCP scaffolds, randomly-oriented PLLA nanofibrous membranes, sandblasting with large grit and acid-etching treated titanium substrates, BTO NPs/P(VDF-TrFE) nanocomposite membranes and left-handed phenylalanine chiral hydrogels exhibited predominantly osteoinductive function, whereas the aligned PLLA nanofibrous membranes and right-handed phenylalanine chiral hydrogels exhibited superior adipoinductive function. These results are consistent with the results of traditional evaluation methods and the results of previous studies and revealed the phenylalanine chiral hydrogel's potential in chondrogenic reg ulation.[35a,b,36b,c,41] More importantly, MeD-P yields excellent accuracy and reliability in the evaluation of osteo-inductive and adipo-inductive biomaterials at as early as the first week of MSCs culture, which is much quicker than the time required for conventional cellular staining techniques such as ARS staining. Moreover, the experimental process is simpler, more economical, and environmentally friendly, as compared to other evaluation techniques such as immunofluorescence and qPCR. The artificial intelligence-based assessment model can comprehensively evaluate the tri-lineage differentiation probabilities of stem cells regulated by the materials, which is consistent with the practical reality of complex interactions between biomaterials and cells in vivo. Notably, data processing methods have taken the experimental batch effects across laboratories and materials into consideration, so MeD-P is batch-independent and easily implemented for further evaluation of biomaterials.

Nevertheless, further improvements are required for MeD-P to extend its functions. Considering the limitations of gene expression data in representing the precise cell differentiation state, we will take the potential effects of other omics data such as proteomics and methylomics into account.[42] Moreover, opinions of researchers on the exact timepoints at which cells start to display their transcriptomic features are inconsistent, so the earliest harvesting timepoints for effective prediction by MeD-P therefore need to be clarified in further research depending on the characteristics of biomaterials. We would do more work in testing MeD-P using various biomaterials at even earlier timepoints. Furthermore, sophisticated and specialized materiomic analysis tools are required to keep pace with increasing biomaterial-derived data. Parameterizing the physicochemical properties of materials would be helpful for understanding the relationship between the physicochemical parameters of materials and their biological potential.[1a,13b] In future, researchers will be invited to use MeD-P or add their RNA-seq and physicochemical data. The expansion of the regenerative biomaterial RNA-seq database will play an important role in elucidating the biological mechanisms of biomaterial-driven tissue regeneration. This has much potential in deciphering the physicochemical parameters of biomaterials that influence lineage-specific MSCs differentiation, thus facilitating the progress of biomaterial design strategies.

4. Conclusion

Overall, this study offers a convenient tool, MeD-P, for the identification of MSCs lineage fate directions, thereby providing an efficient, cost-effective, and batch-independent strategy for the functional evaluation and performance optimization of biomaterials. To the best of our knowledge, this is the first study that reported constructing an artificial intelligence-based assessment model based on RNA-seq data in the field of biomaterial evaluation. This method provides a convenient way to predict a biomaterial's inductive function on stem cell lineage commitment with high accuracy, and is able to compare data across different laboratories and materials. It has much potential in investigating the complex effects of various physicochemical parameters of biomaterials on MSCs lineage fate regulation. It can also be applied for standardized functional evaluation of biomaterials. Hence, we believe that machine learning-based artificial intelligence strategies can be widely used for standardized functional biomaterial evaluation, which could hasten the progress of regenerative medicine research.

5. Experimental Section

RNA-seq Data Collection: Public RNA-seq datasets related to the tri-lineage differentiation of hMSCs (osteogenesis, chondrogenesis, and adipogenesis) were collected from the Gene Expression Omnibus (GEO, http://www.ncbi.nlm.nih.gov/geo/) and ArrayExpress (https://www.ebi.ac.uk/arrayexpress/) repository. Twelve transcriptome datasets meeting the following requirements were included: 1) Transcriptome data were obtained based on next-generation sequencing technology; 2) Raw

© 2023 Wiley-VCH GmbH

15214095, 2023, 19, Downloaded from https://onlinelibrary.wiley.com/doi/10.1002/adma.202210637 by Peking University Health, Wiley Online Library on [21/07/2023]. See the Terms and Conditions (https://onlinelibrary.wiley.com/terms-and-conditions) on Wiley Online Library for rules of use; OA articles are governed by the applicable Creative Commons License

.fastq format sequencing data were saved in the database; 3) There were sequencing data both before and after the induction of differentiation; 4) The hMSCs used in the induction experiments must meet the minimal criteria of MSCs, including i) the ability to self-renew, ii) multipotency with osteogenic, chondrogenic, and adipogenic differentiation potentials, which were verified by conventional staining methods such as Alizarin Red S staining, Oil Red O staining, and Alcian Blue staining, and iii) expression of a characteristic set of canonical MSC surface markers, such as CD73, CD90, and CD105, while lacking expression of CD14, CD34, CD45, and human leukocyte antigen-DR (HLA-DR).

RNA-seq Data Preprocessing: Raw *.fastq* data were filtered with fastp (version 0.20.1) software to remove adapters, low-quality sequences, and repetitive sequences.[43] The rRNA sequences were then removed using bowtie2 (version 2.4.2) software with default settings.[44] Clean data were obtained as *.fastq* format. STAR (version 2.7.6a) software was then used to align the clean data to the genome (Homo sapiens, GRCh38),[45] resulting in generation of the *.bam* file. The featureCounts function in the Subread (version 2.0.1) software was used to count the number of reads aligned to a gene or transcript,[46] to obtain a quantitative expression matrix at the transcript level. Finally, the transcripts were converted into gene names according to the Ensemble ID, and the average of multiple transcripts corresponding to the same gene was calculated and rounded up to obtain the raw count matrix at the gene level. The data format is $N^{m1\times n}$, where N is a natural number, $m1$ is the number of genes, and n is the number of samples.

Unqualified Sample Screening: Hierarchical cluster analysis was used to screen unqualified samples by distinguishing the data dissimilarity based on the whole-genome gene expression matrix. The dissimilarity was calculated by Euclidean distance among samples, and the agglomeration method was set as "average." The hclust function in R package stats (version 3.6.1) was applied to generate a cluster dendrogram,[47] where the samples above the manual cut-off redline were supposed to be outliers and excluded in further analyses.

Allocation of Training, Validation, and Testing Data Sets: Five RNA-seq datasets were selected out of the twelve public RNA-seq datasets to feed the machine learning models. These samples were further divided into various splits of the training and validation sets by random sampling, which was referred to as cross-validation,[48] for the purpose of training and optimizing the parameters in the machine learning models. Briefly, 70% of samples in each cell type within the training datasets were randomly selected as the training set, while the remaining samples were collected as the validation set. The other seven RNA-seq datasets were used as the testing set for benchmarking the performance of the machine learning models.

Batch Effect Adjustment: The methods were different between the training datasets and testing datasets. For the five training datasets, the ComBat_seq function in the R package ComBat-seq was used to adjust the raw gene expression count matrix to fit with the estimated "batch-free" negative binomial distribution,[49] where the group parameter was set as sample class, and the batch parameter was set as dataset accession. The DaMiR.normalization and DaMiR.SVadjust function in the R package DaMiRseq was then successively used to adjust the gene expression distribution at the sample level and the confounding factors related to batch effects.[50] The format of the adjusted gene expression matrix was $Q+^{m2\times n}$, where Q+ is a positive rational number, $m2$ is the number of genes after filtering low-abundance expressed genes, and n is the number of samples in the training datasets. By combination and optimization of ComBat-seq and DaMiRseq, the training datasets were adjusted in both the gene expression distribution within biological replicates using the negative binomial regression model and the library sizes among samples across batches using variance stabilizing transformation (VST).[51] For the seven testing datasets, the gene expression matrices were adjusted separately. In detail, by taking one of the seven testing datasets as an example, the ComBat_seq function in the R package ComBat-seq was used to adjust the raw gene expression count matrix, which was integrated by the specific testing dataset and five training datasets, where the group parameter was set as "*NULL*," and the batch parameter was set as dataset accession. Then the DaMiR.iTSnorm function in the R package DaMiRseq was applied to adjust the testing dataset at the sample level, using the gene expression distribution of samples in the training datasets as references. Similarly, other testing datasets were adjusted individually. Notably, the parameters concerning the sample classes were always set as unknown when adjusting the testing datasets. So that the batch effect between the testing data and the training data could be identified and adjusted by the algorithms without manual interference.

Feature Selection and Extraction: The DESeqDataSetFromMatrix function in the R package DESeq2 was applied on the adjusted training data matrix to identify differentially expressed genes among the three differentiation lineage directions of hMSCs.[52] For example, in the case of osteogenesis-specific feature selection, the osteogenic samples were set as the experimental group, and the other three classes (chondrogenesis, adipogenesis, undifferentiated) as the control group respectively, and selected three gene sets that were highly expressed in the experimental group compared with the three control groups respectively, whereby the fold change was set as greater than 10 and the adjusted p-value was set as less than 0.001. Then the highly expressed osteogenesis-specific gene list was combined by taking the concatenation of the three gene sets. Similarly, feature genes were selected for the other classes. The concatenation of four characteristic gene lists were collected as the overall feature genes. The filter function in the R package tidyverse was then used to extract the characteristic gene expression matrix of samples,[53] and the data format was $Q+^{m3\times n}$, where $m3$ is the number of selected characteristic genes.

Data Visualization: The batchQC function in the R package BatchQC was occupied in the visualization of the gene expression distribution at the sample level with histograms and circular dendrograms.[54] The t-Distributed Stochastic Neighbor Embedding (t-SNE) algorithm was applied for visualizing samples with a 2D plot using the TSNEPlot function in the R package Seurat (version 4.0.5).[55] The visualization of gene expression profiles was implemented using the Heatmap function in the R package ComplexHeatmap.[56] The plot_ly function in the R package plotly was used to visualize the sample clustering in a 3D plot of the principal component analysis (PCA).[57] The hierarchical clustering dendrogram was generated by hclust function in R package stats (version 3.6.1).[47] The normalized gene expression patterns of house-keeping genes and cell-type specific differentiation marker genes were visualized using the qplot function in R package ggplot2 (version 3.3.3).[58]

Machine Learning Models Implementation and Cross-Validation: Nine popular multi-class machine learning methods were adopted, which were Support Vector Machine with radial basis function kernel or linear kernel (SVM-R and SVM-L), Random Forest (RF), Gaussian Naive Bayes (GNB), Linear Discriminant Analysis (LDA), Logistic Regression (LR), Multi-layer Perceptron (MLP), RidgeClassifierCV (RidgeCV), and k-nearest neighbors (kNN). Models were iteratively trained and optimized based on the gene expression reference to classify the hMSCs lineage fate directions with modules in the python package sklearn.[59] The hyperparameters of the models were optimized by cross-validation in every single random sampling by learning to fit the classification task.[48]

Performance Evaluation of Machine Learning Models: The performance of nine models (SVM-R, SVM-L, RF, GNB, LDA, LR, MLP, RidgeCV, kNN) on identifying unknown data was evaluated using accuracy, f1-score, precision, recall, specificity, and the area under the receiver operating characteristic (ROC) curve (AUROC).[33,60] These overall and per-class metrics were calculated on adjusted testing datasets. In particular, for the per-class metrics, a binary classifier for each class was implemented with the one-versus-rest method.[25] In binary classification tasks, the result of the model on one sample could be one of four cases: the positive sample be predicted as positive (True Positive, TP), the positive sample be predicted as negative (False Negative, FN), the negative sample be predicted as positive (False Positive, FP), and the negative sample be predicted as negative (True Negative, TN).[60] The accuracy of a model referred to the proportion of the correctly predicted samples (TP+TN) in the overall samples (TP+TN+FP+FN). Precision referred

© 2023 Wiley-VCH GmbH

15214095, 2023, 19, Downloaded from https://onlinelibrary.wiley.com/doi/10.1002/adma.202210637 by Peking University Health, Wiley Online Library on [21/07/2023]. See the Terms and Conditions (https://onlinelibrary.wiley.com/terms-and-conditions) on Wiley Online Library for rules of use; OA articles are governed by the applicable Creative Commons License

to the proportion of the samples that the model correctly predicts as positive (TP) in the total samples that the model predicts as positive (TP+FP). Recall was the proportion of the samples that the model correctly predicted as positive (TP) in the total samples that were actually positive (TP+FN). The *f*1-score was defined as the harmonic mean of precision and recall, that is, the reciprocal of the average of the reciprocals of precision and recall. The specificity, also known as the true negative rate, was the proportion of the samples correctly predicted to be negative by the model (TN) in the total samples that were actually negative (TN+FP). The formulas are as listed below:

$$\text{Accuracy} = \frac{\text{TP}+\text{TN}}{\text{TP}+\text{TN}+\text{FP}+\text{FN}} \tag{1}$$

$$\text{Precision} = \frac{\text{TP}}{\text{TP}+\text{FP}} \tag{2}$$

$$\text{Recall} = \frac{E}{\text{TP}+\text{FN}} \tag{3}$$

$$f1-\text{score} = \frac{2\times\text{precision}\times\text{recall}}{\text{precision}+\text{recall}} \tag{4}$$

$$\text{Specificity} = \frac{\text{TN}}{\text{TN}+\text{FP}} \tag{5}$$

For multi-class classification tasks like the task in this study, the overall *f*1-score and accuracy were the same value. The basis is as follows:[34]

Let *K* be the number of categories. TP, FP, TN, and FN denoted the sample number of True Positive, False Positive, True Negative, and False Negative, respectively, and the subscript *i* denoted the category to which they belong.

$$\text{The total number of samples is}: \text{Total} = \sum_{i=1}^{K}\left(\text{TP}_i+\text{FN}_i\right) = \sum_{i=1}^{K}\left(\text{TP}_i+\text{FN}_i\right) \tag{6}$$

$$\text{Accurary} = \frac{\sum_{i=1}^{K}\text{TP}_i}{\text{Total}} \tag{7}$$

$$\text{Micro}-\text{average precision}\, P_{\text{micro}} = \frac{\sum_{i=1}^{K}\text{TP}_i}{\sum_{i=1}^{K}\left(\text{TP}_i+\text{FP}_i\right)} = \frac{\sum_{i=1}^{K}\text{TP}_i}{\text{Total}} \tag{8}$$

$$\text{Micro}-\text{average recall}\, R_{\text{micro}} = \frac{\sum_{i=1}^{K}\text{TP}_i}{\sum_{i=1}^{K}\left(\text{TP}_i+\text{FN}_i\right)} = \frac{\sum_{i=1}^{K}\text{TP}_i}{\text{Total}} \tag{9}$$

$$\text{Micro}-\text{average}\ f1-\text{score}\, F_{\text{micro}} = \frac{2P_{\text{micro}}\times R_{\text{micro}}}{P_{\text{micro}}+R_{\text{micro}}} \tag{10}$$

From the four equations above, it can be obtained: $F_{\text{micro}} = P_{\text{micro}} = R_{\text{micro}} = \text{Accuracy}$.

The Classification Visualization module in the python package Yellowbrick was used to visualize the per-class accuracy, precision, recall, and *f*1-score with the classification report and confusion matrix.[61]

Fabrication of 3D-Printed β-TCP Scaffolds: 3D-printed *β*-TCP scaffolds were fabricated using 3D-printing technique based on protocols described in previous study.[41] In detail, 1.8 g *β*-TCP powders, 0.1 g sodium alginate powders (Alfa Aesar, low viscosity), and 1.8 g of Pluronics F-127 solution (20 wt%, Sigma-Aldrich, USA) were mixed and homogeneously stirred to prepare injectable *β*-TCP inks. Then *β*-TCP scaffolds were generated by 3D scaffold printer (Dresden, Germany) using *β*-TCP inks via a dosing pressure of 1.5–2.5 bar and a moving speed of 3 mm s^{-1}. The 3D-printed *β*-TCP scaffolds were dried at room temperature for 24 h and then sintered at 1100 °C for 3 h.

Fabrication of Electrospun PLLA Nanofibrous Membranes: Aligned (AL) and randomly-oriented (RD) PLLA nanofibrous membranes were fabricated using electrospinning techniques, based on protocols described in previous study.[36b] 1.4 g PLLA powders and 20 mL of trifluoroethanol were mixed and stirred overnight to prepare the precursor solution. Then the solution was loaded into a 20 mL syringe with a steel needle (inner diameter: 0.5 mm) and ejected at a rate of 0.7 mL h^{-1} using a programmable syringe pump (Top 5300, Japan). An unremitting voltage (16 kV) was provided to the tip of the needle along with ejecting fluids using high-voltage equipment (DW-P303–1AC, China). Meanwhile, a metal plate (20–25 cm^2) was used as a collector at a distance of 15 cm from the tip of the needle to obtain randomly-oriented PLLA nanofibrous membranes and a cylindrical drum, which rotated at a surface linear rate of 12 m s^{-1}, was used to obtain aligned PLLA nanofibrous membranes. Then all nanofibrous membranes were kept in a vacuum oven (DZF- 6210, Bluepard, China) at room temperature for 2 weeks for solvent volatilizing.

Fabrication of Sandblasting with Large Grit and Acid-Etching Treated Ti-6Al-4V Substrates: White corundum with a particle size of 250–300 µm was used to sandblast the pure titanium substrates uniformly at a distance of 3–5 cm under standard atmospheric pressure. Then samples were ultrasonically cleaned with acetone, anhydrous ethanol, and deionized water for 10 min and dried. Subsequently, the sandblasted titanium substrates were placed in an acid etching solution mixed with an equal volume of 18% HCl and 48% H_2SO_4 at 60 °C for 30 min. Then substrates were ultrasonically cleaned with deionized water 3 times for 15 min each time and placed in a vacuum oven at 55 °C for 12 h. Ti-6Al-4V substrates with polished surfaces were prepared as a control.

Fabrication of BTO NPs/P(VDF-TrFE) Nanocomposite Membranes: Electroactive BTO NPs/P(VDF-TrFE) nanocomposite membranes were fabricated using film-casting and corona poling techniques.[35a] BTO NPs (99.9%, average particle size of 100 nm, Alfa Aesar) were first dispersed by ultrasonication in 0.01 mol L^{-1} of dopamine hydrochloride (99%, Alfa Aesar) aqueous solution and stirred for 12 h at 60 °C to obtain polydopamine-modified BTO NPs. For the fabrication of nanocomposite membranes, 0.356 g polydopamine-modified BTO NPs and 2 g P(VDF-TrFE) (65/35 mol% VDF/TrFE) copolymer powders were dispersed in 20 mL of *N*,*N*-dimethylformamide (DMF) by ultrasonic treatment for 3 h, followed by stirring overnight, to form a stable suspension. The suspension was then cast into membranes on a particular glass and dried at 55 °C for 12 h to remove residual solvent. For polarization treatment, the BTO NPs/P(VDF-TrFE) nanocomposite membranes were placed in the center area of the metal stage of the corona polarimeter, at a distance of 20 mm with the electrode head whose loading voltage was set as 20 kV. Each sample was polarized for 30 min.

Fabrication of Phenylalanine Chiral Hydrogel: Phenylalanine chiral hydrogel matrices were fabricated using self-assembly techniques.[35b] Briefly, 6.0 g D-phenylalanine methyl ester hydrochloride (Aladdin Chemicals, China) was dissolved in a mixture of 8.0 mL of triethylamine (Et3N, Aladdin Chemicals, China) and 100 mL of dry dichloromethane (DCM, Sigma-Aldrich, America) and stirred at room temperature for 24 h. Then 2.6 g 1,4-benzenedicarbonyl dichloride in 20 mL of dry DCM was added dropwise to the solution. After evaporating solvents, the residues were subsequently dissolved in 100 mL of ethanol. After filtration, the undissolved substance was collected and dried to obtain *p*-Ph-(D-Phe-OMe)$_2$ (5.3 g). Then 10 mL of aqueous NaOH (2.0 M) was added to a suspension of 3.0 g *p*-Ph-(D-Phe-OMe)$_2$ in 20 mL of methanol and stirred for 24 h. The solution was then acidified with 3.0 M HCl until achieving a pH value less than 3.0 to form a gel sediment. Then the gel was washed with deionized water, and dried in a vacuum oven for 12 h to produce *p*-Ph-(D-Phe-OH)$_2$ (2.6 g, D-Phenylalanine chiral hydrogel matrices). Similarly, *p*-Ph-(L-Phe-OH)$_2$ was prepared (2.8 g, L-Phenylalanine chiral hydrogel matrices).

Characterization, Culture, and Tri-Lineage Differentiation Induction of hBM-MSCs: Primary human BM-MSCs used in biological experiments were purchased from and characterized by Cyagen Bioscience Inc. (Guangzhou, China). Cryopreserved hBM-MSCs in passage 2 were thawed and then cultured in mesenchymal stem cell medium (MSCM, ScienCell, USA) supplemented with 5% v/v fetal bovine serum (FBS), 1% v/v growth supplements (MSCGS), and 100 IU mL^{-1} penicillin–streptomycin

© 2023 Wiley-VCH GmbH

15214095, 2023, 19, Downloaded from https://onlinelibrary.wiley.com/doi/10.1002/adma.202210637 by Peking University Health, Wiley Online Library on [21/07/2023]. See the Terms and Conditions (https://onlinelibrary.wiley.com/terms-and-conditions) on Wiley Online Library for rules of use; OA articles are governed by the applicable Creative Commons License

15214095, 2023, 19, Downloaded from https://onlinelibrary.wiley.com/doi/10.1002/adma.202210637 by Peking University Health, Wiley Online Library on [21/07/2023]. See the Terms and Conditions (https://onlinelibrary.wiley.com/terms-and-conditions) on Wiley Online Library for rules of use; OA articles are governed by the applicable Creative Commons License

at 37 °C and 5% CO_2. The culture medium was changed every 2–3 days. Upon reaching 80–90% confluence, hBM-MSCs were detached with 0.25% w/v trypsin/ethylenediaminetetraacetic acid (EDTA) (Gibco). The cells from the third to fifth passages were used in this study. The surface antigen expression of hBM-MSCs were characterized by flow cytometry analysis using the OriCell human MSC analysis kit (Cyagen Bioscience Inc., Guangzhou, China) following the manufacturer's protocol, including the utilization of fluorescein isothiocyanate (FITC)–conjugated antibodies specific to cell surface antigens CD29, CD166, CD105, CD73, CD44, CD14, CD45 CD34, CD11b, and HLA-DR. The data were analyzed using NovoExpress 1.4.1. According to the manufacturer's instructions, osteogenic, chondrogenic, and adipogenic induction were carried out using mesenchymal stem cell osteogenic differentiation medium (MODM, ScienCell, USA), chondrogenic differentiation medium (MCDM, ScienCell, USA), and adipogenic differentiation medium (MADM, ScienCell, USA), respectively. In particular, pellets were formed with 2.5×10^5 cells (500 µL) in each 15 mL conical tube for chondrogenic induction. The tri-lineage differentiation potential of hBM-MSCs were validated by Alizarin Red S (ARS), Oil Red O staining on D14 after osteogenic or adipogenic induction, and Alcian Blue staining on D21 after chondrogenic induction.

Cell Seeding on Biomaterials: 3D-printed β-TCP scaffolds, PLLA nanofibrous membranes, sandblasted and acid-etched Ti-6Al-4V alloy substrates, and BTO NPs/P(VDF-TrFE) nanocomposite membranes were placed in 6-well or 24-well plates after cobalt-60 irradiation and disinfection. 200~500 µL of complete medium was added to each well for pre-infiltration for 2 h to facilitate cell adhesion. hBM-MSCs from the third to fifth passages were digested with trypsin and uniformly seeded on the surface of the biomaterials or the pore structure of the scaffolds at a density of 2×10^5 cells mL^{-1} after suspension, and then incubated at 37 °C in a humidified atmosphere with 5% CO_2. The culture medium was changed every 2–3 days.

Cell Seeding in 3D Phenylalanine Chiral Hydrogel Matrices: hBM-MSCs suspension (1×10^6 cells mL^{-1}) were initially encapsulated within a concentrated solution of the hydrogel matrices gelator (final gelator concentration: 3 mg mL^{-1}) in DMSO (final DMSO concentration: 3.3% v/v). The self-supporting matrices were formed within several minutes. Then, more complete medium was added to the matrices and incubated under standard culture conditions (37 °C, 5% CO_2). The culture medium was changed every 2–3 days.

Total RNA Extraction, Library Construction, and Transcriptome Sequencing: After differentiation induction or incubation with biomaterials, hBM-MSCs were harvested in Trizol (Ambion) on day 7 of culture. Total RNA from MSCs was extracted using an RNAprep Pure Kit for Cell/Bacteria (TIANGEN) according to the manufacturer's instructions. The quality of purified RNA was checked by NanoDrop ND-1000 (NanoDrop, Wilmington, DE, USA). A high-throughput paired-end RNA sequencing library was constructed according to the standard Illumina mRNA library preparation protocol (Illumina, Inc.). Sequencing was performed according to the paired-end DNA sequencing protocols from Illumina on an HiSeq6000 system with a paired-end module (Illumina, Inc.). A total of 150 bp were sequenced from each side of a fragment that was ≈300 bp in length.

Differentiation Scores Calculation: As shown in Table S1, Supporting Information, 95 canonical marker genes related to the osteogenesis, chondrogenesis, adipogenesis, and undifferentiated state of hMSCs were obtained based on the literature review and their presence in the adjusted training gene expression matrix. The expression characteristics of these genes are listed in Data file S4, Supporting Information, as the supplement to Table S1, Supporting Information, concerning the tri-lineage differentiation of hMSCs. The marker gene expression profiles of biomaterial-induced hMSCs were extracted using the filter function in the R package tidyverse. The AddModuleScore module in Seurat (version 4.0.5) was used to obtain the osteogenic, chondrogenic, adipogenic differentiation, and undifferentiated scores of samples by calculating the average canonical marker gene expression levels of each cell type.

Batch Effect Adjustment for Biomaterial-Generated RNA-seq Data: The gene expression matrix was adjusted separately for each biomaterial. Likewise, the ComBat_seq function in the R package ComBat-seq was used to adjust the raw gene expression count matrix that integrated the independent testing dataset with training datasets,[49] where the group parameter was set as "*NULL*," and the batch parameter was set as the dataset accessions. Then the DaMiR.iTSnorm function in the R package DaMiRseq (version 1.10.0) was used to adjust the testing dataset at the sample level according to the gene expression distribution of samples in the training datasets.[50] Notably, the parameter concerning the sample classes was set as unknown in adjusting the testing datasets.

Physicochemical Characterization of Biomaterials: The surface morphologies and molecular structures of biomaterials were characterized by field emission scanning electron microscopy (FE-SEM, S-4800, HITACHI, Japan). The elemental maps were obtained by Energy dispersive spectrometer (EDS) in the mapping mode. The surface roughness of the sandblasted and acid-etched Ti-6Al-4V alloy substrates was analyzed by white light interferometer (ContourGT-I, Bruker, America). The diffraction pattern of the β-TCP scaffolds was examined by X-ray diffraction (XRD) to analyze its crystal structure. For the electrical property characterization, the membranes were first treated by corona poling under a DC field of 13 kV at room temperature for 30 min. The quantitative analysis of the surface potential distribution was evaluated by Kelvin Probe Force Microscopy using commercially available Pt-coated Si probes (SCM-PIT, Bruker, America). The hysteresis loop was analyzed using a commercial ferroelectric analyzer setup (TF1000, aix ACCT Systems GmbH, Germany) with a maximum field amplitude of 4 kV mm^{-1} at a frequency of 0.5 Hz. For the degradability evaluation, the 3D printed β-TCP scaffolds were immersed in Tris-HCl (pH = 7.4) buffer at 37 °C with the ratio of solvent volume and mass at 200 mL g^{-1} for 1, 3, 5, 7, 14, and 21 days. The concentrations of Ca and P elements in the collected solutions were measured using an inductively coupled plasma emission spectrometer (ICP-OES, Agilent 5110, Agilent, America). Three parallel samples were used to obtain the average value.

Alizarin Red S, Oil Red O, Alcian Blue, and Alkaline Phosphatase Staining: Cultured cells were fixed at the indicated time points with 4% w/v paraformaldehyde for 30 min and stained with Alizarin Red S (1% w/v solution in water; pH 4.2, Solarbio), Oil Red O (300 mg mL^{-1} Oil Red O in isopropanol diluted 60:40 in water, Sigma-Aldrich) for 30 min and washed several times with water. Chondrogenic pellets were fixed with 4% w/v paraformaldehyde for 30 min, eluted using an ethanol gradient, embedded in paraffin, sliced into 4 µm sections, and further stained with Alcian Blue for 15 min. Microscopy images were obtained using a 10×, 20×, or 40× phase-contrast objective on a Leica DM IRB/E microscope. Alizarin Red S and Oil Red O staining was quantified by extracting the color in isopropanol and measuring the absorbance at 520 nm. ALP staining was performed using a nitro blue tetrazolium (NBT) and 5-bromo-4-chloro-3-indolyl phosphate (BCIP) (NBT/BCIP) staining kit (Solarbio).

Immunofluorescence Analysis: After culturing on biomaterials for 3 days, hBM-MSCs were rinsed in phosphate-buffered saline (PBS) and fixed in 4% w/v paraformaldehyde for 15 min. After fixation, the samples were washed three times with PBS for 5 min each time. Then, samples were then permeabilized with 0.1% w/v Triton X-100 (diluted with PBS) for 10 min and blocked with 3% w/v bovine serum albumin (BSA; diluted with PBS) for 1 h to minimize non-specific staining. After removal of the permeabilization solution, samples were rinsed and washed with PBS again. The above procedures were carried out at room temperature. The samples were then incubated with the primary antibody—rabbit anti-BMP2 antibody (1:100; ab214821; abcam) in 3% w/v BSA overnight at 4 °C. After thorough rinsing with PBS to remove excess antibodies, the cells were incubated with goat anti-rabbit IgG H&L (Alexa Fluor 488) pre-adsorbed secondary antibody (2 µg mL^{-1}; ab150081; abcam) for 1 h in darkness. 4′,6-Diamidino-2-phenylindole (DAPI; Sigma) was used to stain the cell nuclei. TRITC-labeled phalloidin was used to stain the cytoskeletal f-actin. Images of three random fields of vision were captured with a confocal laser scanning microscope (Leica).

Quantitative Real-Time PCR Analysis: After differentiation induction, total cellular RNA from hBM-MSCs were harvested using Trizol (Ambion) on D7 of culture according to the manufacturer's instructions.

 © 2023 Wiley-VCH GmbH

Amplifications were then performed with different primers. The quality and quantity of the RNA obtained were subjected to spectrophotometric analysis using a bio-photometer (Thermo Scientific NanoDrop8000). The RNA was then reversed-transcribed into complementary DNA (cDNA) using a Reverse Transcription kit (Takara Bio Inc., Japan). Quantitative real-time polymerase chain reaction (RT-qPCR) was performed using the SYBR Green PCR reagent kit (Roche, Germany) on an ABI QuantStudio 3 Real-Time PCR System (Applied Biosystems, Foster City, CA, USA). The data were analyzed using QuantStudio Design and Analysis Desktop software (Thermo Fisher Scientific). The primer sequences are listed in Table S2, Supporting Information. All gene expression values were normalized to glyceraldehyde-3-phosphate dehydrogenase (*GAPDH*) expression.

Statistical Analysis: R (version 3.6.1 and 4.1.1) was used for RNA-seq data processing and data visualization. Python (version 3.9.1) was used for machine learning training and benchmarking. All quantitative biological experimental data were expressed as mean ± standard deviation (SD). Statistical analysis was performed using the GraphPad Prism 6.01 software. Statistical differences were evaluated using Student's *t*-test for independent samples. Differences between groups with $*p < 0.05$, $**p < 0.01$, or $***p < 0.001$ were considered as statistically significant.

Supporting Information

Supporting Information is available from the Wiley Online Library or from the author.

Acknowledgements

Y.Z., X.P., and Y.G. contributed equally to this work. This work was supported by the National Key Research and Development Program of China (2022YFC2401803, 2021YFB3800800, 2018YFE0194400), the National Natural Science Foundation of China (Nos. 82022016, 82221003, 52273258, 81991505, 51973004, U22A20160), and the Beijing Municipal Natural Science Foundation (7222226). The authors also thank Prof. Chengtie Wu and Dr. Xiaopeng Yu at the Shanghai Institute of Ceramics, Chinese Academy of Sciences for providing 3D-printed β-TCP scaffolds for testing the model.

Conflict of Interest

The authors declare no conflict of interest.

Data Availability Statement

The data that support the findings of this study are available from the corresponding author upon reasonable request.

Keywords

artificial intelligence, gene expression pattern, lineage fate, machine learning, mesenchymal stem cells, regenerative biomaterials

Received: November 16, 2022
Revised: February 2, 2023
Published online: March 18, 2023

[1] a) W. L. Murphy, T. C. McDevitt, A. J. Engler, *Nat. Mater.* **2014**, *13*, 547; b) N. Mitrousis, A. Fokina, M. S. Shoichet, *Nat. Rev. Mater.* **2018**, *3*, 441; c) E. S. Place, N. D. Evans, M. M. Stevens, *Nat. Mater.* **2009**, *8*, 457.

[2] a) B. Roson-Burgo, F. Sanchez-Guijo, C. Del Cañizo, J. De Las Rivas, *BMC Genomics* **2016**, *17*, 944; b) R. E. B. Fitzsimmons, M. S. Mazurek, A. Soos, C. A. Simmons, *Stem Cells Int.* **2018**, *2018*, 8031718; c) A. Arthur, S. Gronthos, *Int. J. Mol. Sci.* **2020**, *21*, 9759.

[3] a) J. Le, L. Zhongqun, W. Zhaoyan, S. Yijun, W. Yingjin, W. Yaojie, J. Yanan, J. Zhanrong, M. Chunyang, G. Fangli, X. Nan, Z. Lingyun, W. Xiumei, W. Qiong, L. Xiong, S. Xiaodan, *Bioact. Mater.* **2021**, *6*, 613; b) V. V. Hiew, S. F. B. Simat, P. L. Teoh, *Stem Cell Rev. Rep.* **2018**, *14*, 43.

[4] L. Zhou, V. O. Gjvm, J. Malda, M. J. Stoddart, Y. Lai, R. G. Richards, K. Ki-wai Ho, L. Qin, *Adv. Healthcare Mater.* **2020**, *9*, e2001008.

[5] P. K. Nguyen, D. Nag, J. C. Wu, *Adv. Drug Delivery Rev.* **2010**, *62*, 1175.

[6] a) B. P. Hung, J. N. Harvestine, A. M. Saiz, T. Gonzalez-Fernandez, D. E. Sahar, M. L. Weiss, J. K. Leach, *Biomaterials* **2019**, *189*, 1; b) G. Abagnale, M. Steger, V. H. Nguyen, N. Hersch, A. Sechi, S. Joussen, B. Denecke, R. Merkel, B. Hoffmann, A. Dreser, U. Schnakenberg, A. Gillner, W. Wagner, *Biomaterials* **2015**, *61*, 316; c) R. Mayeux, *NeuroRx* **2004**, *1*, 182.

[7] C. Thermes, *Trends Genet.* **2014**, *30*, 418.

[8] a) P. Munch Danzon, W. G. Manning, M. S. Marquis, *Health Care Financ. Rev.* **1984**, *5*, 23; b) F. H. Wians, *Lab Med.* **2009**, *40*, 105; c) Y. Zhu, R. Huang, Z. Wu, S. Song, L. Cheng, R. Zhu, *Nat. Commun.* **2021**, *12*, 2614.

[9] a) J. Goecks, V. Jalili, L. M. Heiser, J. W. Gray, *Cell* **2020**, *181*, 92; b) M. Ashraf, M. Khalilitousi, Z. Laksman, *Curr. Protoc.* **2021**, *1*, e261; c) S. J. Maceachern, N. D. Forkert, *Genome* **2021**, *64*, 416.

[10] a) F. Buggenthin, F. Buettner, P. S. Hoppe, M. Endele, M. Kroiss, M. Strasser, M. Schwarzfischer, D. Loeffler, K. D. Kokkaliaris, O. Hilsenbeck, T. Schroeder, F. J. Theis, C. Marr, *Nat. Methods* **2017**, *14*, 403; b) B. Schmauch, A. Romagnoni, E. Pronier, C. Saillard, P. Maillé, J. Calderaro, A. Kamoun, M. Sefta, S. Toldo, M. Zaslavskiy, T. Clozel, M. Moarii, P. Courtiol, G. Wainrib, *Nat. Commun.* **2020**, *11*, 3877.

[11] P. Liang, W. Yang, X. Chen, C. Long, L. Zheng, H. Li, Y. Zuo, *Mol. Ther. Nucleic Acids* **2020**, *20*, 155.

[12] a) D. Soriano-Valdez, I. Pelaez-Ballestas, A. Manrique de Lara, A. Gastelum-Strozzi, *Clin. Rheumatol.* **2021**, *40*, 11; b) A. L. Beam, I. S. Kohane, *J. Am. Med. Assoc.* **2018**, *319*, 1317.

[13] a) N. Groen, M. Guvendiren, H. Rabitz, W. J. Welsh, J. Kohn, J. de Boer, *Acta Biomater.* **2016**, *34*, 133; b) D. G. A. J. Hebels, A. Carlier, M. L. J. Coonen, D. H. Theunissen, J. de Boer, *Biomaterials* **2017**, *149*, 88.

[14] A. Rauch, A. K. Haakonsson, J. G. S. Madsen, M. Larsen, I. Forss, M. R. Madsen, E. L. Van Hauwaert, C. Wiwie, N. Z. Jespersen, M. Tencerova, R. Nielsen, B. D. Larsen, R. Röttger, J. Baumbach, C. Scheele, M. Kassem, S. Mandrup, *Nat. Genet.* **2019**, *51*, 716.

[15] N. P. T. Huynh, B. Zhang, F. Guilak, *FASEB J.* **2019**, *33*, 358.

[16] X. Yi, P. Wu, J. Liu, S. He, Y. Gong, J. Xiong, X. Xu, W. Li, *Mol. Omics* **2021**, *17*, 790.

[17] P. Lutsik, A. Baude, D. Mancarella, S. Öz, A. Kühn, R. Toth, J. Hey, U. H. Toprak, J. Lim, V. H. Nguyen, C. Jiang, A. Mayakonda, M. Hartmann, F. Rosemann, K. Breuer, D. Vonficht, F. Grünschläger, S. Lee, M. K. Schuhmacher, D. Kusevic, A. Jauch, D. Weichenhan, J. Zustin, M. Schlesner, S. Haas, J. H. Park, Y. J. Park, U. Oppermann, A. Jeltsch, F. Haller, et al., *Nat. Commun.* **2020**, *11*, 5414.

[18] J. Vijay, M. F. Gauthier, R. L. Biswell, D. A. Louiselle, J. J. Johnston, W. A. Cheung, B. Belden, A. Pramatarova, L. Biertho, M. Gibson, M. M. Simon, H. Djambazian, A. Staffa, G. Bourque, A. Laitinen, J. Nystedt, M. C. Vohl, J. D. Fraser, T. Pastinen, A. Tchernof, E. Grundberg, *Nat. Metab.* **2020**, *2*, 97.

© 2023 Wiley-VCH GmbH

15214095, 2023, 19, Downloaded from https://onlinelibrary.wiley.com/doi/10.1002/adma.202210637 by Peking University Health, Wiley Online Library on [21/07/2023]. See the Terms and Conditions (https://onlinelibrary.wiley.com/terms-and-conditions) on Wiley Online Library for rules of use; OA articles are governed by the applicable Creative Commons License

[19] K. Futrega, P. G. Robey, T. J. Klein, R. W. Crawford, M. R. Doran, *Commun. Biol.* **2021**, *4*, 29.
[20] A. W. Robert, A. B. B. Angulski, L. Spangenberg, P. Shigunov, I. T. Pereira, P. S. L. Bettes, H. Naya, A. Correa, B. Dallagiovanna, M. A. Stimamiglio, *Sci. Rep.* **2018**, *8*, 4739.
[21] H. Li, F. F. Masieri, M. Schneider, T. Kottek, S. Hahnel, K. Yamauchi, D. Obradović, J. K. Seon, S. J. Yun, R. A. Ferrer, S. Franz, J. C. Simon, B. Lethaus, V. Savković, *Cells* **2020**, *9*, 2069.
[22] M. J. Peffers, K. Goljanek-Whysall, J. Collins, Y. Fang, M. Rushton, J. Loughlin, C. Proctor, P. D. Clegg, *PLoS One* **2016**, *11*, e0160517.
[23] L. Li, C. Zhang, J. ling Chen, F. fan Hong, P. Chen, J. fu Wang, *Cell Prolif.* **2019**, *52*, e12539.
[24] S. Brielle, D. Bavli, A. Motzik, Y. Kan-Tor, X. Sun, C. Kozulin, B. Avni, O. Ram, A. Buxboim, *Proc. Natl. Acad. Sci. U. S. A.* **2021**, *118*, e2016322118.
[25] J. H. Hong, S. B. Cho, *Neurocomputing* **2008**, *71*, 3275.
[26] Z. Jin, J. Shang, Q. Zhu, C. Ling, W. Xie, B. Qiang, in *Web Information Systems Engineering – WISE 2020. WISE 2020. Lecture Notes in Computer Science*, vol. *12343*, Springer, Cham **2020**, p. 503.
[27] H. Zhang, in *Proc. 17th Int. Florida Artificial Intelligence Research Society Conference FLAIRS 2004*, AAAI Press, Menlo Park **2004**, p. 562.
[28] A. Tharwat, T. Gaber, A. Ibrahim, A. E. Hassanien, *AI Commun.* **2017**, *30*, 169.
[29] J. C. Stoltzfus, *Acad. Emerging Med.* **2011**, *18*, 1099.
[30] I. Lorencin, N. Anđelić, J. Španjol, Z. Car, *Artif. Intell. Med.* **2020**, *102*, 101746.
[31] C. Peng, Q. Cheng, *IEEE Trans. Neural Networks Learn. Syst.* **2021**, *32*, 2595.
[32] Z. Zhang, *Ann. Transl. Med.* **2016**, *4*, 218.
[33] J. D. Novaković, A. Veljović, S. S. Ilić, Ž. Papić, T. Milica, *Theory Appl. Math. Comput. Sci.* **2017**, *7*, 39.
[34] M. Grandini, E. Bagli, G. Visani, arXiv:2008.05756, v1 **2020**.
[35] a) X. Zhang, C. Zhang, Y. Lin, P. Hu, Y. Shen, K. Wang, S. Meng, Y. Chai, X. Dai, X. Liu, Y. Liu, X. Mo, C. Cao, S. Li, X. Deng, L. Chen, *ACS Nano* **2016**, *10*, 7279; b) Y. Wei, S. Jiang, M. Si, X. Zhang, J. Liu, Z. Wang, C. Cao, J. Huang, H. Huang, L. Chen, S. Wang, C. Feng, X. Deng, L. Jiang, *Adv. Mater.* **2019**, *31*, 1900582; c) M. E. Klontzas, S. Reakasame, R. Silva, J. C. F. Morais, S. Vernardis, R. J. MacFarlane, M. Heliotis, E. Tsiridis, N. Panoskaltsis, A. R. Boccaccini, A. Mantalaris, *Acta Biomater.* **2019**, *88*, 224.
[36] a) Y. Takahashi, M. Yamamoto, Y. Tabata, *Biomaterials* **2005**, *26*, 3587; b) W. Liu, Y. Wei, X. Zhang, M. Xu, X. Yang, X. Deng, *ACS Nano* **2013**, *7*, 6928; c) S. L. Luo, Z. H. Yang, M. Lin, X. Xu, Y. H. Zhang, B. Guo, L. L. Dong, *Adv. Mater. Res.* **2014**, *926–930*, 965.
[37] a) H. Savoji, B. Godau, M. S. Hassani, M. Akbari, *Front. Bioeng. Biotechnol.* **2018**, *6*, 86; b) S. Abdulghani, G. R. Mitchell, *Biomolecules* **2019**, *9*, 750; c) Y. Liu, X. Zhang, C. Cao, Y. Zhang, J. Wei, Y. jun Li, W. Liang, Z. Hu, J. Zhang, Y. Wei, X. Deng, *Adv. Funct. Mater.* **2017**, *27*, 1703771.
[38] H. Amani, H. Arzaghi, M. Bayandori, A. S. Dezfuli, H. Pazoki-Toroudi, A. Shafiee, L. Moradi, *Adv. Mater. Interfaces* **2019**, *6*, 1900572.
[39] Y. H. Wang, Y. Liu, P. Maye, D. W. Rowe, *Biotechnol. Prog.* **2006**, *22*, 1697.
[40] a) V. Bunpetch, X. Zhang, T. Li, J. Lin, E. P. Maswikiti, Y. Wu, D. Cai, J. Li, S. Zhang, C. Wu, H. Ouyang, *Biomaterials* **2019**, *192*, 323; b) O. Chaudhuri, J. Cooper-White, P. A. Janmey, D. J. Mooney, V. B. Shenoy, *Nature* **2020**, *584*, 535.
[41] L. Chen, C. Deng, J. Li, Q. Yao, J. Chang, L. Wang, C. Wu, *Biomaterials* **2019**, *196*, 138.
[42] a) E. Lin, H. Y. Lane, *Biomarker Res.* **2017**, *5*, 2; b) P. S. Reel, S. Reel, E. Pearson, E. Trucco, E. Jefferson, *Biotechnol. Adv.* **2021**, *49*, 107739.
[43] S. Chen, Y. Zhou, Y. Chen, J. Gu, *Bioinformatics* **2018**, *34*, i884.
[44] B. Langmead, S. L. Salzberg, *Nat. Methods* **2012**, *9*, 357.
[45] A. Dobin, C. A. Davis, F. Schlesinger, J. Drenkow, C. Zaleski, S. Jha, P. Batut, M. Chaisson, T. R. Gingeras, *Bioinformatics* **2013**, *29*, 15.
[46] a) Y. Liao, G. K. Smyth, W. Shi, *Bioinformatics* **2014**, *30*, 923; b) Y. Liao, G. K. Smyth, W. Shi, *Nucleic Acids Res.* **2013**, *41*, e108.
[47] E. Paradis, J. Claude, K. Strimmer, *Bioinformatics* **2004**, *20*, 289.
[48] L. Liu, M. Tamer Özsu, *Encyclopedia of Database Systems*, Springer Nature, Switzerland **2020**.
[49] Y. Zhang, G. Parmigiani, W. E. Johnson, *NAR: Genomics Bioinf.* **2020**, *2*, lqaa078.
[50] M. Chiesa, G. I. Colombo, L. Piacentini, *Bioinformatics* **2018**, *34*, 1416.
[51] S. Anders, W. Huber, *Genome Biol.* **2010**, *11*, R106.
[52] M. I. Love, W. Huber, S. Anders, *Genome Biol.* **2014**, *15*, 550.
[53] H. Wickham, M. Averick, J. Bryan, W. Chang, L. McGowan, R. François, G. Grolemund, A. Hayes, L. Henry, J. Hester, M. Kuhn, T. Pedersen, E. Miller, S. Bache, K. Müller, J. Ooms, D. Robinson, D. Seidel, V. Spinu, K. Takahashi, D. Vaughan, C. Wilke, K. Woo, H. Yutani, *J. Open Source Software* **2019**, *4*, 1686.
[54] S. Manimaran, H. M. Selby, K. Okrah, C. Ruberman, J. T. Leek, J. Quackenbush, B. Haibe-Kains, H. C. Bravo, W. E. Johnson, *Bioinformatics* **2016**, *32*, 3836.
[55] A. Butler, P. Hoffman, P. Smibert, E. Papalexi, R. Satija, *Nat. Biotechnol.* **2018**, *36*, 411.
[56] Z. Gu, R. Eils, M. Schlesner, *Bioinformatics* **2016**, *32*, 2847.
[57] C. Sievert, Chapman and Hall/CRC, **2020**, https://plotly-r.com.
[58] R. A. M. Villanueva, Z. J. Chen, *Meas. Interdiscip. Res. Perspect.* **2019**, *17*, 160.
[59] D. K. Barupal, O. Fiehn, *J. Mach. Learn. Res.* **2011**, *12*, 2825.
[60] D. Chicco, G. Jurman, *BMC Genomics* **2020**, *21*, 6.
[61] B. Bengfort, R. Bilbro, *J. Open Source Software* **2019**, *4*, 1075.

© 2023 Wiley-VCH GmbH

15214095, 2023, 19, Downloaded from https://onlinelibrary.wiley.com/doi/10.1002/adma.202210637 by Peking University Health, Wiley Online Library on [21/07/2023]. See the Terms and Conditions (https://onlinelibrary.wiley.com/terms-and-conditions) on Wiley Online Library for rules of use; OA articles are governed by the applicable Creative Commons License